

Rakel Næss

CFD Simulations of Open and Closed Sand Trap Design for Tonstad Hydropower Plant

Master's thesis in Civil and Environmental Engineering

Supervisor: Kaspar Vereide

June 2020

NTNU
Norwegian University of Science and Technology
Faculty of Engineering
Department of Civil and Environmental Engineering

Rakel Næss

CFD Simulations of Open and Closed Sand Trap Design for Tonstad Hydropower Plant

Master's thesis in Civil and Environmental Engineering
Supervisor: Kaspar Vereide
June 2020

Norwegian University of Science and Technology
Faculty of Engineering
Department of Civil and Environmental Engineering



Preface

This master thesis was written at the Norwegian University of Science and Technology (NTNU), Department of Civil and Environmental Engineering (IBM) during the spring of 2020. The work was performed in cooperation with Sira-Kvina power company. The main objective of this master thesis was to perform numerical simulations of Sand trap 3 at Tonstad hydropower plant in two configurations. The work has been challenging, but most of all educational and valuable for my future career.

I would like to thank my supervisor and Adjunct Associate Professor Kaspar Vereide for the opportunity to join such an interesting project, and my co-supervisors Ola Haugen Havrevoll and Elena Pummer for their support and guidance. I would also like to thank Dipl.-Ing. Dr. techn. Wolfgang Richter at Graz University of Technology for valuable inputs regarding the numerical model.

Finally, I would like to thank my fellow students and my family for the support throughout this period.

Trondheim, 10.06.2020

Rakel Næss

Abstract

In this master thesis, Computational Fluid Dynamics (CFD) was used to simulate Sand trap 3 at Tonstad hydropower plant in the current configuration and reconstructed with horizontal shear plates. The operators of the power plant observed sediment problems when the capacity was increased along with the installation of a fifth turbine. The simulations are based on the geometry of this sand trap, and the numerical simulations are carried out to investigate the effect of upgrading the sand trap by installing horizontal shear plates.

It is given an introduction to sand trap, sediment transport and CFD theory. The theory chapters are followed by the procedure for numerical modelling with Ansys Fluent, including creating the geometry, mesh generation and setting up the models.

Two different cases are simulated to study the effect of installing horizontal shear plates in the sand trap. Steady state Reynolds-Averaged Navier-Stokes (RANS) simulations were run to compare the flow behaviour with and without shear plates installed in the sand trap. Transient RANS simulations were carried out to investigate the effect of the shear plates when particles are injected into the sand trap.

The results of the steady state simulations showed that the velocity decreases close to the bed when the sand trap is reconstructed with horizontal shear plates, allowing particles to settle and reducing the entrainment force on the deposits. The transient simulations with injection of particles confirmed that the reduced velocity close to the bed gives better conditions for particle settling. The trap efficiency increases when horizontal shear plates are installed in the sand trap.

It is shown that Ansys Fluent is a suitable CFD software for the modelling of particles in a pressurized sand trap.

Sammendrag

Denne masteroppgaven handler om numerisk modellering (“Computational Fluid Dynamics”, CFD) av Sandfang 3 ved Tonstad kraftverk med dagens utforming og rekonstruert med horisontale ribber. Det ble observert sedimentproblemer i sandfanget etter kapasiteten økte da en femte turbin ble installert. Simuleringene er basert på geometrien for dette sandfanget, og de numeriske simuleringene er gjennomført for å studere effekten av å oppgradere sandfanget ved å installere horisontale ribber.

Det er gitt en innføring i teori om sandfang, sedimenttransport og CFD. Teorikapitlene etterfølges av fremgangsmåten for numerisk modellering med Ansys Fluent, inkludert tillaging av geometrien, generering av grid og oppsett av modellene.

To ulike situasjoner er simulert for å studere effekten av å installere horisontale ribber i sandfanget. Stasjonære “Reynolds-Averaged Navier-Stokes” (RANS) simuleringer ble kjørt for å sammenlikne vannstrømningen med og uten ribber i sandfanget. Transiente RANS simuleringer ble gjennomført for å analysere effekten av ribbene når sedimenter slippes inn i sandfanget.

Resultatene fra de stasjonære simuleringene viste at hastigheten langs bunnen synker når sandfanget rekonstrueres med horisontale ribber. Dette skal i teorien bedre forholdene for sedimentering og redusere medrivningskraften på avsatte sedimenter. De transiente simuleringene med innslipp av sedimenter bekreftet at redusert hastighet langs bunnen gir bedre forhold for sedimentering. Sandfangets fangsteffektivitet øker når horisontale ribber konstrueres i sandfanget.

Det er vist at Ansys Fluent er egnet som CFD-program for modellering av partikler i et trykksatt sandfang.

Table of contents

Preface	i
Abstract	iii
Sammendrag	v
Table of contents	vii
List of figures	x
List of tables	xiii
List of symbols	xv
1 Introduction	1
1.1 Background	1
1.2 Objective	1
1.3 Previous work	2
2 Sand trap and sediment theory	5
2.1 Sand traps	5
2.1.1 Sediments in hydropower tunnels	5
2.1.2 Layout	5
2.1.3 Flow conditions	7
2.1.4 Trap efficiency	9
2.1.5 Design approach	9
2.2 Sediment transport	12
2.2.1 Bed load and suspended load	12
2.2.2 Hjulström diagram	13
2.2.3 Shields diagram	14
2.2.4 Incipient motion of particles in tunnels	16
3 CFD Theory	19
3.1 CFD in hydraulic engineering	19
3.2 Meshing	19
3.3 Governing equations for CFD	21

3.4	Numerical solution techniques	22
3.4.1	The SIMPLEC algorithm	26
3.5	Turbulence modelling	29
3.5.1	The k- ϵ turbulence model	32
3.6	Graphic techniques used in CFD	33
3.7	Error and uncertainty in CFD modelling	34
4	Numerical modelling with Ansys Fluent	38
4.1	Ansys Fluent	38
4.2	Creating the geometry	39
4.3	Mesh generation	41
4.4	Numerical details and simulation settings	43
4.5	Post-processing of the results	47
5	Results	49
5.1	Steady state simulations	49
5.2	Simulations with sediments	57
5.2.1	Simulations with 1 mm particles	57
5.2.2	Simulations with 0.3 mm particles	60
5.2.3	Sand trap efficiency	66
6	Discussion	68
7	Conclusion	71
7.1	Proposals for future work	71
8	References	74
	Appendix	78
	Appendix A	80

List of Figures

1	3D scan of Sand trap 3 at Tonstad power plant.	2
2	General design of an open sand trap.	7
3	General design of a closed sand trap.	7
4	Main sections for a sand trap.	8
5	Particle settling trajectories in a longitudinal section.	10
6	Transport of bed load and suspended load.	12
7	Forces acting on a particle.	13
8	Hjulström diagram (NVE, 2010).	14
9	Shields diagram (Schwimmer, 2012).	15
10	Cell aspect and expansion ratio.	20
11	Element shapes available in Ansys Meshing.	21
12	Discretization molecule.	23
13	Calculation molecule for the Second Order Upwind scheme.	24
14	Estimation of a quantity Φ at side W of cell p with SOU.	24
15	Laminar, transitional and turbulent flow.	29
16	Time averaging for steady (left) and unsteady turbulent flow (right).	31
17	Ansys Workbench.	39
18	Sand trap model.	40
19	Sand trap model with horizontal shear plates.	40
20	Mesh quality - Orthogonal quality.	42
21	Mesh quality - Aspect ratio.	42
22	Mesh quality - Skewness.	42
23	Sediment inlet.	45
24	Residuals for the simulation without shear plates.	49
25	Residuals for the simulation with shear plates.	49
26	Vector overview plot of the velocity along the bed.	50
27	Vector overview plot of the velocity along the symmetry plane.	50
28	Vector plot of the velocity along <i>Part 1</i> of the bed.	51
29	Vector plot of the velocity along <i>Part 1</i> of the symmetry plane.	51

30	Vector plot of the velocity along <i>Part 2</i> of the bed.	52
31	Vector plot of the velocity along <i>Part 2</i> of the symmetry plane.	53
32	Vector plot of the velocity along <i>Part 3</i> of the bed.	53
33	Vector plot of the velocity along <i>Part 3</i> of the symmetry plane.	54
34	Vector plot of the velocity in a cross-section.	55
35	Turbulent kinetic energy along the bed.	55
36	Turbulent kinetic energy along the symmetry plane.	56
37	Injection of 1 mm particles after 20 s.	57
38	Injection of 1 mm particles - after 50 s.	58
39	Injection of 1 mm particles - after 100 s.	59
40	Sediments left in the tunnel after 125 s.	59
41	Injection of 0.3 mm particles - after 20 s.	60
42	Injection of 0.3 mm particles - after 50 s.	61
43	Injection of 0.3 mm particles - after 100 s.	62
44	Injection of 0.3 mm particles - after 200 s.	63
45	Injection of 0.3 mm particles - after 250 s.	63
46	Injection of 0.3 mm particles - after 300 s (end of simulation).	64
47	Sediments left in the tunnel after 215 s (longitudinal view).	65
48	Sediments left in the tunnel after 215 s (plan view).	65

List of Tables

1	Flow types according to Reynolds number.	30
2	Model constants in the k- ϵ turbulence model.	33
3	Errors and uncertainties in CFD.	35
4	Number of mesh elements and nodes.	41
5	Roughness height and roughness constant for the walls and the bed.	44
6	Numerical methods and boundary conditions used in the simulations.	45
7	Sediment injection details.	46
8	Sand trap efficiency.	66

List of symbols

Abbreviations

ADCP	Acoustic Doppler Current Profiler
CFD	Computational Fluid Dynamics
DES	Detached Eddy Simulation
DNS	Direct Numerical Simulation
DPM	Discrete Phase Model
IBM	Department of Civil and Environmental Engineering
LES	Large Eddy Simulation
NTNU	Norwegian University of Science and Technology
RANS	Reynolds-Averaged Navier-Stokes
SIMPLE	Semi-Implicit Method for Pressure Linked Equations
SOU	Second Order Upwind

Greek symbols

α	Horizontal expansion angle	[°]
β	Vertical expansion angle	[°]
γ	Specific weight	[N/m ³]
ϵ	Turbulent dissipation	[m ² /s ³]
η	Trap efficiency	[-]
μ	Dynamic viscosity	[Ns/m ²]
μ_t	Eddy viscosity	
ν	Kinematic viscosity	[m ² /s]

ρ	Density	[kg/m ³]
τ	Shear stress	[N/m ²]

Roman symbols

A	Area	[m ²]
a	Acceleration	[m/s ²]
C	Coefficient	[-]
d	Diameter	[m]
F	Force	[N]
g	Gravitational acceleration	[m/s ²]
h	Height	[m]
I	Slope of the energy line	[-]
k	Turbulent kinetic energy	[m ² /s ²]
L	Length	[m]
m	Mass	[kg]
n	Manning's roughness coefficient	[s/m ^{1/3}]
p	Pressure	[Pa]
Q	Discharge	[m ³ /s]
R	Hydraulic radius	[m]
S	Longitudinal slope	[-]
t	Time	[s]
u	Water velocity	[m/s]
u_*	Shear velocity	[m/s]

w	Settling velocity	[m/s]
W	Submerged particle weight	[N]

Dimensionless numbers

Re	Reynolds number
Re^*	Boundary Reynolds number
τ^*	Shields parameter

Subscripts

0	Bed
cr	Critical
D	Drag
F	Friction
L	Lift
m	Mean
s	Sediment

1 Introduction

1.1 Background

Water used for hydropower often contains mineral particles that enters the tunnel from the intake and brook intakes. Sediments may cause economical losses due to damaged turbines and lost power production. The sediments should therefore be extracted before the water enters the turbine. A common measure to reduce the wear is to construct pressurized sand traps inside the tunnel upstream the turbines.

Tonstad hydropower plant is the largest hydropower plant in Norway in terms of energy production, with an annual average of 3.8 TWh. The power plant is located in the municipality of Sirdal in Agder county in Norway, and is owned and operated by Sira-Kvina power company. In 1988, a fifth turbine was installed in parallel to the four existing turbines, increasing the capacity from 640 to 960 MW. A new sand trap, referred to as Sand trap 3, was constructed in connection with the installation of the fifth turbine. Sand trap 3, located between the surge tank and the pressure shaft, was designed to take care of most of the sediment load. However, increased sediment transport in the tunnel was observed after increasing the capacity, resulting in the need for more frequent emptying and sediments passing through the turbines. The problems are currently solved by enforcing restrictions on the operation of the power plant (Vereide, Svingen and Guddal, 2015).

Computational Fluid Dynamics (CFD) can be used for a wide range of fluid flow problems. It is not only applied to solve problems but also for design and optimizing. CFD will in this work be used to investigate the hydraulic performance of the existing sand trap, and a possible upgrading of the sand trap.

1.2 Objective

This master thesis will look into the building of the sand trap geometry, mesh generation and setup of the CFD model using the software Ansys Fluent. At first, steady flow simulations will be carried out to compare the flow behaviour in the sand trap in

the current configuration and rebuilt with horizontal shear plates. Secondly, simulations with sediment injections will be performed to evaluate the effect of installing horizontal shear plates on the sand trap efficiency. The results will indicate the capability of Ansys Fluent to model particles in pressurized sand traps and provide Sira-Kvina with an initial evaluation of the suggested upgrading of the sand trap.

In 2019, a physical model of Sand trap 3 was constructed at the Hydraulic Laboratory at the Norwegian University of Science and Technology (NTNU). The numerical results were planned to be compared to the results obtained in the physical model for validation. This was not possible as the physical experiments were delayed as a result of the laboratory closing down mid-March due to Covid-19.

1.3 Previous work

Oddmund Brevik (2013) performed steady state and transient simulations of Sand trap 3 at Tonstad power plant to investigate the reason for turbine damages due to sediment transport. Both the case of stationary flow and filling of the sand trap was simulated using the software STAR-CCM+. The results were compared to field measurements. It was found that Detached Eddy Simulation (DES) provides better results where the turbulence is large compared to Reynolds-Averaged Navier-Stokes (RANS). The geometry was created based on data from a laser scan. The scan is shown in Figure 1 (Brevik, 2013).

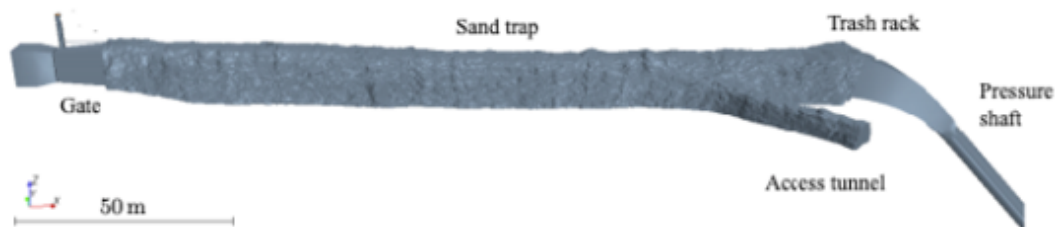


Figure 1: 3D scan of Sand trap 3 at Tonstad power plant.

Kari Bråtveit and Nils Reidar Bøe Olsen (2015) simulated the flow in Sand trap 3 at Tonstad hydropower plant using the software STAR-CCM+. A calibration method for horizontal Acoustic Doppler Current Profilers (H-ADCP) was evaluated based on the results from the CFD simulations. It was found that Reynolds-Averaged Navier-Stokes (RANS) simulations with standard k - ϵ turbulence models can be used for the prediction of the flow field. The results obtained in connection to this study showed that CFD simulations can be used to accurately calibrate H-ADCP.

Wolfgang Richter, Kaspar Vereide and Gerald Zenz (2017) presented the background of the power system situation at Tonstad hydropower plant along with the challenges for the hydraulic system. 3D CFD flow simulations were carried out for Sand trap 3 with the geometry scaled by 1:15. The simulations included two measures for improving the sand trap efficiency: a flow diffuser in the upstream end of the sand trap to reduce the turbulence and an expansion of the cross-section in order to reduce the velocity. It was found that RANS simulations including the sand grain roughness leads to reliable results compared to the results obtained by Brevik (2013). The results showed that the trap efficiency increases with the diffuser and by increasing the cross-section.

Silje Almeland et al. (2019) performed CFD computations with multiple solutions of the Navier-Stokes equations for two different cases involving channel flow into a sand trap. The first case was one of the sand traps at Khimti hydropower plant in Nepal and the second case was Sand trap 3 at Tonstad hydropower plant. The simulations were carried out using the CFD programs SSIIM 1 and OpenFOAM. It was found that the flow pattern changes significantly with changes in discretization schemes, grid resolution and turbulence models. The simulations were validated with laboratory and field measurements.

The four studies mentioned above were carried out in connection to Sand trap 3 at Tonstad hydropower plant. The current thesis differs from the previous work by simulations of the sand trap designed with horizontal shear plates, and simulations with and without particles.

2 Sand trap and sediment theory

2.1 Sand traps

2.1.1 Sediments in hydropower tunnels

Sediments may enter the hydropower tunnel in different ways. Firstly, sediments found in a sand trap could be related to the construction of the tunnel. Unlined tunnels are considered as a standard design in Norway due to high rock quality, with concrete lining or other means of rock support limited to parts of the tunnel to protect against local tunnel collapses or rock falls (Lysne, 1971). During construction, sand and crushed rock is left on the tunnel bed to accommodate transport. The removal of this material may vary from no removal at all to complete manual flushing of the tunnel. The normal requirement is mechanical removal, which results in an approximately 15-20 cm thick layer of sediments on the tunnel bed (Lysne, 1986). The finer sediments will be transported towards the turbines when the power plant is put into operation. The material transport will gradually decrease during the first years of operation, and the coarser material will form a stable cover layer (Eggen, 1973). Sediments may also enter the tunnel from rivers and reservoirs through the intakes, particularly brook intakes (Lysne, 1986) that leads water and sediments directly into the main tunnel.

These sediments should be extracted before the water reaches the turbines. Depending on the size of the particles, sediments may cause damage in the form of erosion, clogging or single-point damage. Smaller particles cause erosion on the mechanical parts and filter clogging, thus decreasing the turbine efficiency and increasing the need for maintenance. Larger particles could cause single-point damage which may result in start-up of cavitation (Vereide et al., 2017). Installing a functional sand trap is a common measure to extract sediments from the turbine water.

2.1.2 Layout

In Norway, sand traps are often placed immediately upstream the lined part of the pressure shafts to collect the sand before it reaches the turbines. This design allows for

unlined tunnels where sand and stone material can be left in the tunnel after construction (Vereide et.al, 2017). By constructing the sand trap downstream of the headrace tunnel, the tunnel itself will function as a sand trap where sediments can settle or change from suspended load to bed load (Roalkvam, 2013).

The idea behind a sand trap is to reduce the velocity allowing particles to settle. Normal practice has been to reduce the velocity by 30 to 50 % at the sand trap (Lysne, 1986) by increasing the cross-sectional area of the tunnel. They can be built either as open sand traps, as illustrated in Figure 2, or as closed sand traps as illustrated in Figure 3 (Vassdragsregulantenenes forening, 1984). An open sand trap is built as an expansion of the headrace tunnel. The idea is to reduce the water velocity, allowing particles to settle, by increasing the tunnel cross-section over the storage area. The cross-sectional area should be increased evenly to avoid separation and turbulence zones. A closed sand trap is constructed with horizontal shear plates that separates the deposits from the flow area. The shear plates reduces or eliminates the requirement to extend the cross-section over the storage space due to the reduced entrainment force on the deposits (Eggen, 1973). The tunnel is expanded at the bottom to obtain the assumed necessary storage volume for the sediments. The spacing between the shear plates should be of the same magnitude as the width of the shear plates, commonly 0.8-1.0 meters (Eggen, 1973). Closed sand traps provides safer storage and better utilization of the storage space. On the other hand, closed sand traps are more expensive to build compared to open sand traps and the sediment removal requires a separate arrangement at some places due to the shear plates.

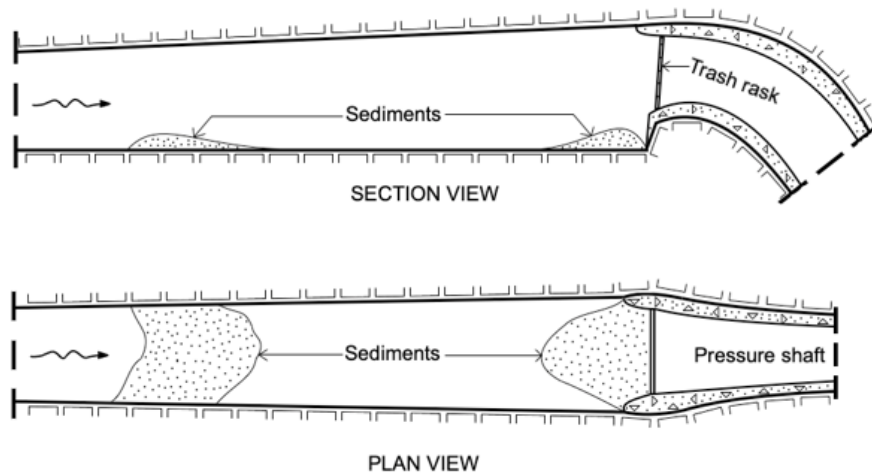


Figure 2: General design of an open sand trap.

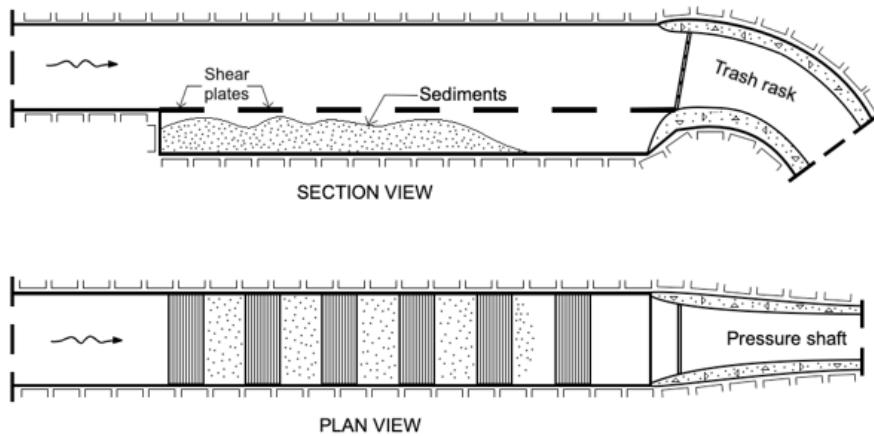


Figure 3: General design of a closed sand trap.

2.1.3 Flow conditions

Deposition of sediments is dependent on the flow conditions in the tunnel and the velocity profile of the water entering the sand trap. If the sand trap is placed in or downstream of a curve, higher velocity along the outside of the bend results in an uneven velocity distribution and reduce the amount of finer sediments being trapped. The trap efficiency will also be affected for sand traps placed in or close to tunnel junctions, due to the formation of eddies and increased turbulence (Lysne, 1971). Sand traps should therefore be placed 100-200 meters downstream of tunnel junctions, curves and gates to ensure an even velocity distribution and a calm flow pattern for the water entering the sand trap (Eggen,

1973). A sand trap is divided into three main sections as shown in Figure 4. Between the inlet channel and the basin, a transition zone is located. The transition zone serves for an even horizontal and vertical expansion over a length required to change from the inlet cross-section to the sand trap cross-section (Paschmann, 2018). If this transition is too abrupt, the flow will not follow the tunnel profile which will result in flow separation and turbulence (Eggen, 1973). The recommendations on horizontal (α) and vertical expansion angle (β) of the transition zone is dependent on the objective. A horizontal expansion angle $\alpha < 4^\circ$ is ideal to prevent flow separation within the expansion, and angles in the range of $4^\circ < \alpha < 5^\circ$ are favourable for jets forming along one of the side walls (Paschmann, 2018).

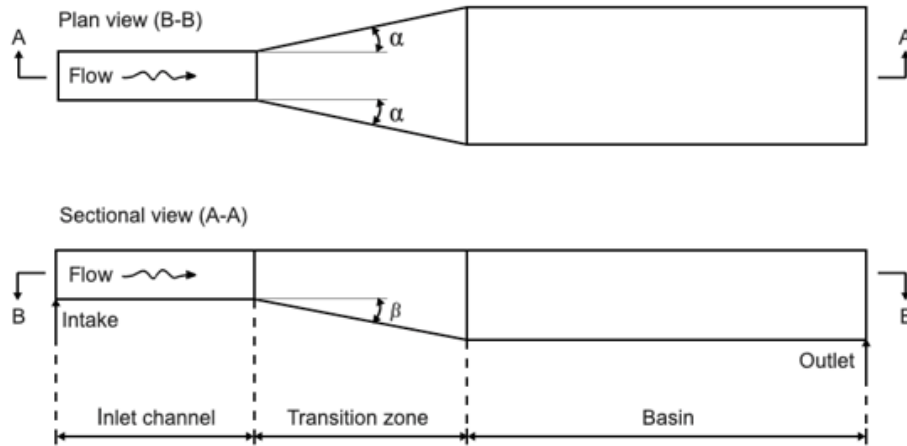


Figure 4: Main sections for a sand trap.

Components to guide and tranquilize the flow can be applied in addition to optimize the geometry, and thereby improve the sediment settling efficiency. Guide walls are placed in the transition zone to evenly direct the flow into the basin (Lysne et al., 2003). To homogenize and calm the flow entering the sand trap, tranquilizing racks can be placed in the entrance region. Ingersoll, McKee and Brooks (1956) stated that the inlet channel in general should (i) distribute the inflow uniformly over the basin area, (ii) facilitate horizontal flow paths, (iii) introduce the flow at a minimal turbulence level, and (iv) prevent high bottom flow velocities with regards to particle resuspension.

2.1.4 Trap efficiency

Knowing the amount of sediments passing the turbines is important in order to assess the extent of turbine wear. The trap efficiency η is a measure of the sand trap functionality and performance. The higher the trap efficiency, the better the facility works. The desired value should be determined in the planning stage based on operational demands with respect to hydro-abrasion and flushing or emptying of the sand trap (Paschmann, 2018).

Several approaches exist for defining the sand trap efficiency. In general, the approaches are based on the critical particle size, a reduction of the overall sediment mass or concentration, or a combination. A particle-size related approach considers excluding particles exceeding a defined critical particle size d_{cr} from the turbine water. This critical limit particle size is dependent on requirements from the operator of the sand trap (Paschmann, 2018). The approaches based on sediment mass and concentration are not taking particle sizes into account. A mass related approach is used when the aim is to reduce the overall sediment mass. The trap efficiency can then be calculated based on the sediment masses entering and leaving the sand trap per unit time. The concentration related approach compares the sediment concentration at the inlet and outlet of the sand trap. The trap efficiency is calculated as follows, where Φ represents the mass (Ranga Raju et al., 1999) or the concentration:

$$\eta = 1 - \frac{\Phi_{s,out}}{\Phi_{s,in}} \quad (1)$$

The approach based on Ranga Raju et al. (1999) will be further used for calculating the sand trap efficiency.

2.1.5 Design approach

Several approaches exist for the design of sand traps. The approach after Camp (1936) aims to find the required basin length when all particles larger or equal to a critical limit

particle size d_{cr} are excluded from the turbine water. The following simplifying assumptions are made for the approach: (i) the flow direction is horizontal and both direction and velocity are constant in every part of the basin, (ii) all particles maintain their shape, size and orientation, meaning constant settling velocity for each particle, (iii) the longitudinal velocity of the particles is equal to the flow velocity and (iv) no resuspension of particles that strikes the bottom (Camp, 1936).

Considering these assumptions, each particle will settle in a straight line as illustrated in the following figure. Assuming entrance at the water surface, particles with size $d > d_{cr}$ settle faster, whilst particles of size $d < d_{cr}$ are not excluded during basin passage (Paschmann, 2018). The following figure, based on Paschmann (2018), shows parallel settling trajectories for particles with $d = d_{cr}$.

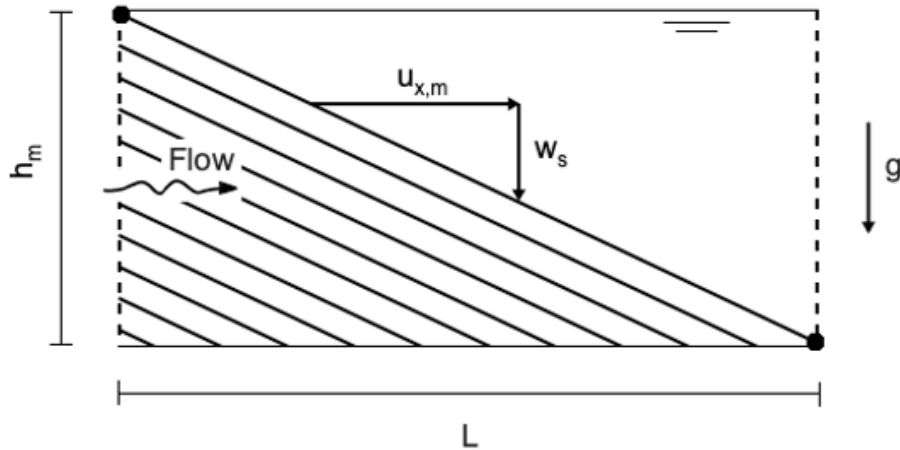


Figure 5: Particle settling trajectories in a longitudinal section.

The settling time for a particle entering the basin at the water surface is expressed as:

$$t_{s,z} = \frac{h_m}{w_s} \quad (2)$$

where h_m is the mean basin flow depth [m] and w_s is the settling velocity for the particles of the defined critical particle size [m/s]. The retention time for a particle entering the

basin is defined as:

$$t_{s,x} = \frac{L}{u_{x,m}} \quad (3)$$

where L is basin length [m] and $u_{x,m}$ is the mean longitudinal flow velocity [m/s] which is calculated based on the continuity equation:

$$u_{x,m} = \frac{Q_d}{A_m} \quad (4)$$

where Q_d is the basin design discharge [m³/s] and A_m is the mean cross-sectional flow area of the basin [m²]. The mean longitudinal flow velocity should be limited to prevent resuspension of deposited particles. The findings of Shields can be used to determine the critical flow velocity corresponding to the desired critical limit particle size, as described in subsection 2.2.3.

Combining Equation 2 and Equation 3 gives the required length of the basin in order to exclude all particles of size equal or greater to the defined critical limit particle size d_{cr} from the turbine water:

$$L = h_m \frac{u_{x,m}}{w_s} \quad (5)$$

2.2 Sediment transport

2.2.1 Bed load and suspended load

Particles up to the size of sand and small stones can be transported with the flow through the waterways in a hydropower system. The mass transport are often divided into two main types according to the way the particles move:

- i. Bed load
- ii. Suspended load

The bed load consist of the coarser fractions which are transported along the bed by sliding, saltating and/or rolling. Suspended load are the finer fractions kept in suspension by the turbulence in the water. The transport mechanisms of bed load and suspended load are illustrated in Figure 6. There are no clear particle size limit that separates the different types of sediment transport. A practical limit for suspension is $u_* > w$, that is, when the shear velocity is greater that the settling velocity of particles (NVE, 2010).

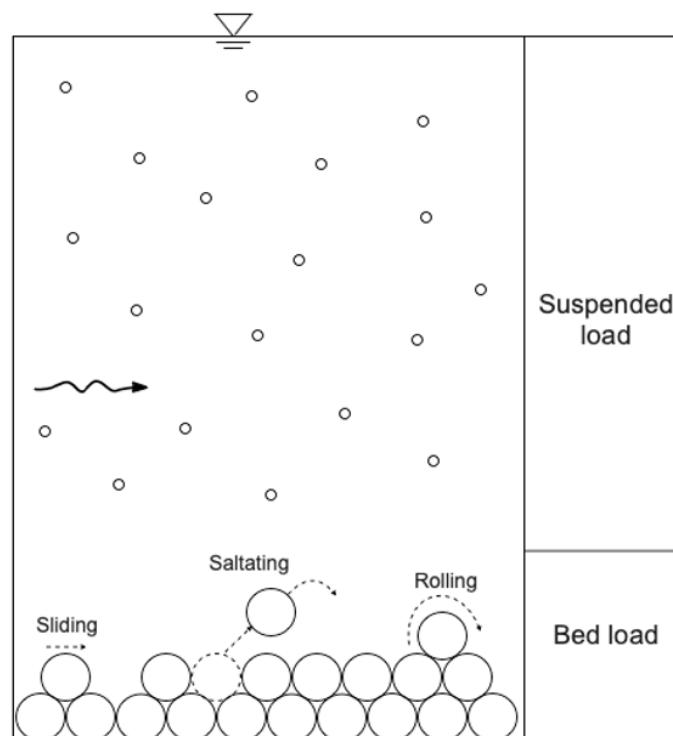


Figure 6: Transport of bed load and suspended load.

Figure 7 shows the forces acting on a particle in flowing water. The driving forces includes the drag and lift force, denoted F_D and F_L . The streamwise drag force is caused by the water pressure on the particle, while the lift force occurs as a result of pressure differences due to velocity variations over the particle. The stabilizing forces are the friction along the bottom, F_F , and the submerged particle weight, W .

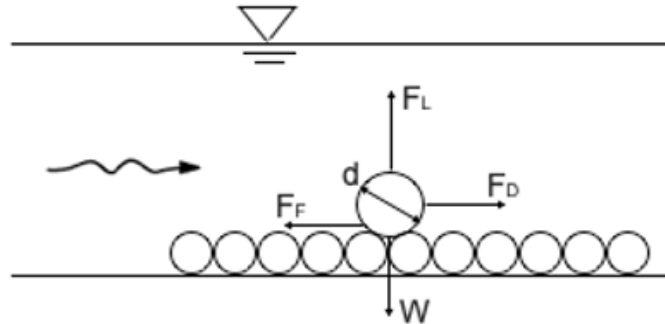


Figure 7: Forces acting on a particle.

By equilibrium, the stabilizing and destabilizing forces can be used to calculate the particle diameter for initiation of movement. However, it is not practically possible to analyze each particle in the water. The transported particle diameter is commonly found graphically or by calculation, as described in the following subsections.

2.2.2 Hjulström diagram

Particle transport can be determined graphically by the use of Hjulström diagram. The diagram depicts the average velocity required for particles of varying sizes to be eroded, transported or deposited. The upper curve shows the critical velocity for erosion as a function of particle size, while the lower curve shows the velocity required for deposition as a function of particle size. The area between the curves gives the velocity and particle size for particles transported in the water. The axes are logarithmic, and the average velocity, \bar{u} , is given in cm/s and the particle diameter, d , is given in mm.

Generally, the required velocity for erosion increases with increasing particle size. However, the left part of the diagram shows that the critical velocity for erosion increases as

the particle diameter decreases. The finest particles require a higher velocity to erode due to cohesive forces (NVE, 2010). This is shown in the diagram, presented in Figure 8, for particles finer than approximately 0.1 mm.

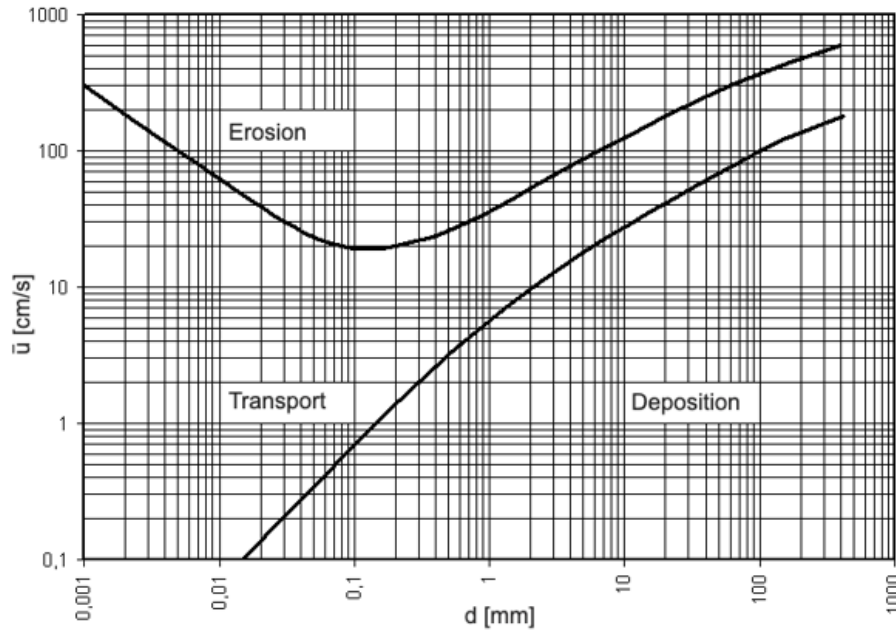


Figure 8: Hjulström diagram (NVE, 2010).

The diagram was made for free surface flows, but a study shows that it also provides good estimates for sediment transport in closed conduits (Roalkvam, 2013).

2.2.3 Shields diagram

Another parameter used to predict sediment transport is the shear stress along the bed. Particles are transported if the bed shear stress exceeds the critical shear stress, τ_{cr} . The critical shear stress is the shear stress required for initiation of motion of particles at the bed. The dimensionless critical shear stress is called Shields parameter, given by:

$$\tau^* = \frac{\tau_0}{(\rho_s - \rho) \cdot g \cdot d_s} \quad (6)$$

where τ_0 is the bed shear stress [N/m²], ρ_s is the density of the sediments [kg/m³],

ρ is the density of water [kg/m³], g is the gravitational acceleration [m/s²] and d_s is the sediment diameter [m].

Shields parameter is represented in the Shields diagram. The curve in the diagram, shown in Figure 9, is a function of the boundary Reynolds number, Re^* , given by the following equation:

$$Re^* = \frac{u_* \cdot d_s}{\nu} \quad (7)$$

$$u_* = \sqrt{g \cdot R \cdot I} = \sqrt{\frac{\tau_0}{\rho}} \quad (8)$$

where u_* is the shear velocity [m/s], d_s is the sediment diameter [m], ν is the kinematic viscosity of water [m²/s], R is the hydraulic radius [m] and I is the slope of the energy line [-].

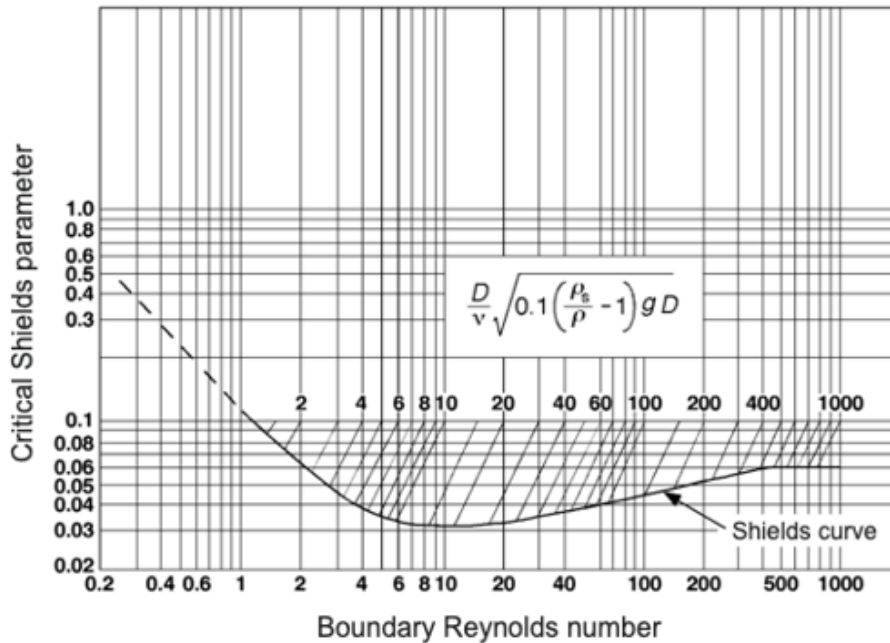


Figure 9: Shields diagram (Schwimmer, 2012).

The Shields diagram for initiation of motion empirically shows the relationship between the dimensionless critical shear stress and the boundary Reynolds number. The diagram

depicts the limit between no sediment motion and initiation of sediment motion, that is, under and over Shields curve, respectively.

2.2.4 Incipient motion of particles in tunnels

So far, the theory presented on sediment transport is based on free surface flow. However, the general flow conditions for both channels and tunnels are fairly well understood. It is a reasonable assumption that the theory of incipient motion derived for rivers and channels should also apply, with some modifications, for tunnels (Lysne, 1969). A great number of equations exist for determining the limiting tractive force for sand particles in flowing water, among others the equation by Shields. These equations are basically identical (Lysne, 1969) and can be written:

$$d = \frac{\tau_0}{(\gamma_s - \gamma) \cdot C} \quad (9)$$

where d is the particle diameter [m], τ_0 is the bed shear stress [N/m^2], γ_s is the specific weight of sediments [N/m^3], γ is the specific weight of water [N/m^3] and C is a coefficient [-]. Introducing the formula for bed shear stress and Manning's formula:

$$\tau_0 = \gamma \cdot R \cdot S \quad (10)$$

$$u = \frac{1}{n} \cdot R^{\frac{2}{3}} \cdot S^{\frac{1}{2}} \longrightarrow S = \frac{u^2 \cdot n^2}{R^{\frac{4}{3}}} \quad (11)$$

where S is the longitudinal slope [-], and n is the Manning's roughness coefficient [$\text{m}/\text{s}^{1/3}$]. The following substitution is applied for tunnels:

$$R = K \cdot A^{\frac{1}{2}} \quad (12)$$

where K is a coefficient [-] and A is the cross-sectional area [m^2]. Combining Equation 9,

10, 11 and 12 gives the following expression for critical particle size in a tunnel:

$$d = \frac{\gamma}{\gamma_s - \gamma} \cdot \frac{u^2}{C' \cdot A^{\frac{1}{6}}} \quad (13)$$

$C' = \frac{C \cdot K^{1/3}}{n^2}$ is a coefficient $[(\text{m}^{1/3}/\text{s})^2]$. In the fundamental study carried out by Lysne in 1969, laboratory experiments and field data confirmed a C' value of approximately 130. Later experience has indicated that C' is varying in the range 115 to 140 (Lysne, 1986).

3 CFD Theory

3.1 CFD in hydraulic engineering

Hydraulic problems have previously often been solved by the use of physical models. It is a time consuming investigation method, and the physical models are scaled down due to limitations in cost and laboratory space. Downscaling of a hydraulic system is associated with scale effects, resulting in non-identical force ratios between the prototype and the model (Paschmann, 2018). Scaling problems occur, amongst others, when simulating very small particles. In contrast, CFD-modelling allows for simulating complex fluid flow problems without downscaling.

Computational Fluid Dynamics (CFD) is the application of numerical techniques used to solve fluid problems by means of computer-based simulation. CFD-modelling provides a significant reduction in time and cost compared to physical model studies as the geometry and the model parameters easily can be varied. Moreover, the ability to study very large systems and systems under hazardous conditions at and beyond their normal performance limits are unique advantages of CFD (Versteeg and Malalasekera, 2007). However, several challenges and limitations are associated with CFD modelling. It is a computationally expensive tool in terms of memory and storage, and the results of a CFD simulation are never 100 % reliable. Proper numerical approaches and methods must be applied to solve the equations efficiently and sufficient knowledge is therefore required to carry out the simulations. Approximations and simplifications introduces errors and deviations from the reality. Errors and uncertainties in CFD modelling are described in section 3.7.

3.2 Meshing

In CFD, a mesh is formed when the fluid domain is divided into smaller subdomains, called cells or elements. A mesh, or a grid, is a discrete representation of the domain and the equations for unknown variables are solved for each cell (Olsen, 2017). The accuracy and convergence of a CFD simulation is dependent on the number of elements and the mesh quality. Increasing the number of elements may result in higher accuracy, but at

the expense of increased computational cost. An essential part of the meshing process is therefore to find the balance between the required solution accuracy and the available computational resources.

The quality can be assessed based on the orthogonality and the aspect and expansion ratio. The orthogonality relates to how close the angle between adjacent element faces are to the optimal angle. The optimal angle is 90° for quadrilateral faces and 60° for triangular faces. For non-orthogonal grids, the grid lines should not intersect at angles below 45° or over 135° . Low non-orthogonality is preferable due to more rapid convergence and in some cases better accuracy (Olsen, 2017). The orthogonality measure ranges from 0 to 1, where 1 implies good quality. Figure 10 shows two grid cells, A and B, from which the aspect ratio and the expansion ratio can be described.

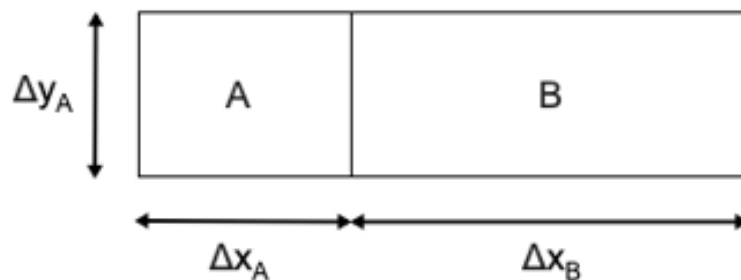


Figure 10: Cell aspect and expansion ratio.

The aspect ratio is a measure of the stretching of an element. It is defined as the ratio of the cell width to its height, $\Delta x_A/\Delta y_A$. The aspect ratio is equal to 1 for an equilateral element, and should not exceed 40 for tetrahedral elements. The expansion ratio, also called smoothness, is defined as $\Delta x_A/\Delta x_B$. Ideally, the expansion ratio should not be larger than around 1.2 to ensure a gradual change in element size, thus avoiding problems for the water flow calculation.

Another measure of the grid quality is the skewness ratio of the elements. The skewness determines how close to ideal the element is. Skewed elements may decrease the accuracy and destabilize the solution (Ansys Fluent). The skewness ratio ranges from 0 to 1, where 1 indicates a completely degenerate cell. A skewness value of 0 is ideal.

The elements in a mesh can have various shapes. The choice depends on the problem, the required accuracy and the solver capabilities. The different mesh element shapes available in Ansys Meshing are illustrated in Figure 11. The use of hexahedral elements gives a uniform mesh and requires fewer elements to obtain the same level of accuracy compared to tetrahedral meshes. Tetrahedral elements can be applied for complex geometries and the generation of a tetrahedral mesh can be done automatically.

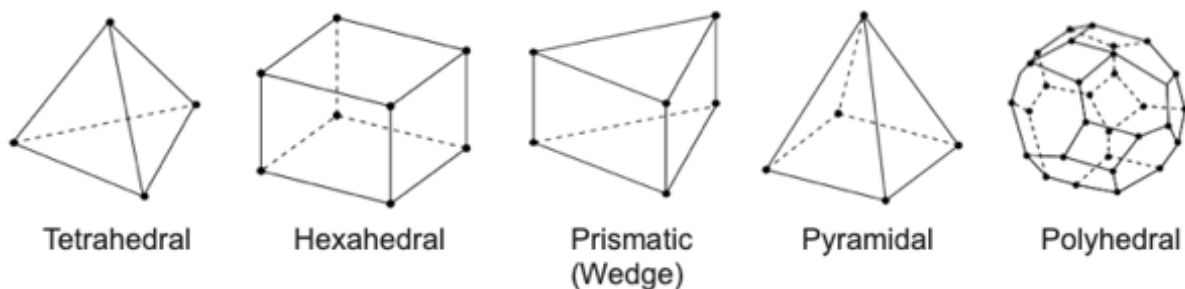


Figure 11: Element shapes available in Ansys Meshing.

3.3 Governing equations for CFD

All of CFD is based on the fundamental governing equations of fluid dynamics, that is, the continuity, momentum and energy equations. The equations represent three physical principles that forms the basis of fluid dynamics (Anderson, 1995):

1. Mass is conserved
2. Newton's second law, $F = ma$
3. Energy is conserved

These physical principles can be expressed in terms of mathematical equations, commonly as integral equations or partial differential equations. Mass conservation requires that the mass inflow rate equals the mass outflow rate. This principle is expressed by the three dimensional continuity equation:

$$\frac{\partial \rho}{\partial t} + \frac{\partial(\rho u)}{\partial x} + \frac{\partial(\rho v)}{\partial y} + \frac{\partial(\rho w)}{\partial z} = \frac{\partial \rho}{\partial t} + \rho \frac{\partial u_i}{\partial x_i} = 0 \quad (14)$$

The density ρ is constant for an incompressible flow, and the continuity equation may be written:

$$\frac{\partial u_i}{\partial x_i} = 0 \quad (15)$$

Newton's second law for fluids states that the rate of change of momentum equals the sum of the resultant forces acting on the fluid body. This is described by the momentum equation, also known as the Navier-Stokes equations. The equations can be written on the following form:

$$\rho \frac{\partial u_i}{\partial t} + \rho u_j \frac{\partial u_i}{\partial x_j} = -\frac{\partial p}{\partial x_i} + \mu_t \frac{\partial^2 u_i}{\partial x_j^2} \quad (16)$$

The left hand side of Equation 16 consist of a transient and a convective term. The right hand side represents the forces, and consist of a pressure term and a diffusive term.

The energy equation states that the rate of change of energy is equal to the rate of work done on a fluid plus the rate of heat addition (Versteeg and Malalasekera, 2007). For thermal studies, the Navier Stokes may be coupled to the principle of energy conservation. This is not relevant for the thesis and will not be further discussed.

3.4 Numerical solution techniques

In order to solve the Navier-Stokes equations by the means of a computer, they must be transferred into a discretized form. There exists three main types of discretization methods: finite difference, finite element and finite volume method. The finite volume method is introduced in the following, as it is applied in most CFD programs including

Ansys Fluent.

Steady convection and diffusion of a general quantity Φ is governed by the following equation (Versteeg and Malalasekera, 2007):

$$\frac{\partial}{\partial x}(\rho u \Phi) = \frac{\partial}{\partial x} \left(\Gamma \frac{\partial \Phi}{\partial x} \right) \quad (17)$$

where the left side of the equation is the convective term and the right side is the diffusive term. Discretization is the process of transferring a partial differential equation into a new equation where the variable in one cell is a function of the variable in the neighbor cell (Olsen, 2017). The new equation is then a weighted average of the quantities in the neighboring cells:

$$\Phi_p = \frac{a_w \Phi_w + a_e \Phi_e + a_n \Phi_n + a_s \Phi_s}{a_p} \quad (18)$$

Where the notations w , e , n and s denotes the neighboring cells in direction west, east, north and south as shown in the discretization molecule in Figure 12.

a_w : weighting factor for cell w

a_e : weighting factor for cell e

a_n : weighting factor for cell n

a_s : weighting factor for cell s

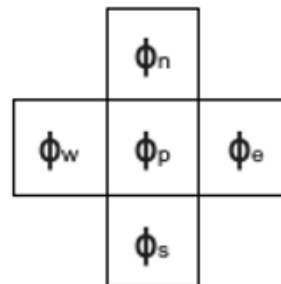


Figure 12: Discretization molecule.

Ansyes Fluent stores discrete values of the quantity Φ at the cell centers. However, the values at the cell faces must be obtained for the convective terms. The values are interpolated from the values in the center of the cell, a process accomplished using an upwind scheme (Ansyes Fluent).

The upwind schemes are numerical discretization methods for solving partial differential equations. Upwinding means that the quantity at the cell surface is derived from the quantity in the cell upstream, or “upwind”. The upwind schemes takes into account the flow direction when determining the value at a cell face. For the First Order Upwind scheme, the quantities at cell faces are determined from only one upstream cell. The quantity at the cell face is then taken to be equal to the quantity in the upstream cell. The scheme assumes that the center values in a cell represent the cell average and holds through the entire cell (Ansys Fluent). When second-order accuracy is desired, the Second Order Upwind (SOU) method is used to calculate quantities at cell faces. The quantities at a cell face is then determined from the two upstream cells, resulting in a nine-point calculation molecule as shown in Figure 13.

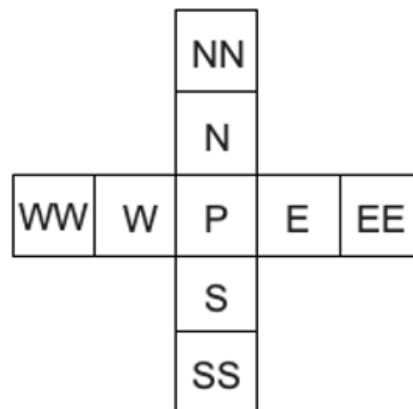


Figure 13: Calculation molecule for the Second Order Upwind scheme.

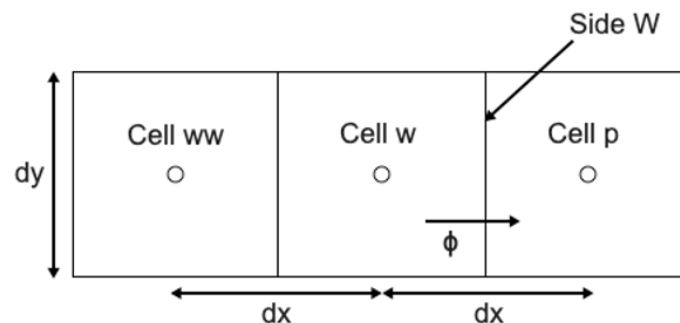


Figure 14: Estimation of a quantity Φ at side W of cell p with SOU.

The Second Order Upwind scheme uses the quantities in cell ww , denoted Φ_{ww} and cell w ,

denoted Φ_w , to extrapolate linearly to side W . The expression for Φ on side W , denoted Φ^w , is then obtained by triangulation (Olsen, 2017):

$$\frac{\Phi^w - \Phi_{ww}}{dx + 0.5dx} = \frac{\Phi_w - \Phi_{ww}}{dx} \longrightarrow \Phi^w = \frac{3}{2}\Phi_w - \frac{1}{2}\Phi_{ww} \quad (19)$$

Considering the transport Equation 17, the convective and diffusive flux are calculated as $u \cdot A \cdot \Phi$ and $\Gamma \cdot A \cdot d\Phi/dx$, respectively. Based on Equation 19, the flux through the west side of cell P is the given in Equation 20. Similarly, the fluxes through the other sides are given in Equation 21-23 (Olsen, 2017):

$$F_w = u_w A_w \left(\frac{3}{2}\Phi_w - \frac{1}{2}\Phi_{ww} \right) + \Gamma_w A_w \frac{\Phi_w - \Phi_p}{dx} \quad (20)$$

$$F_e = u_e A_e \left(\frac{3}{2}\Phi_p - \frac{1}{2}\Phi_w \right) + \Gamma_e A_e \frac{\Phi_p - \Phi_e}{dx} \quad (21)$$

$$F_n = u_n A_n \left(\frac{3}{2}\Phi_n - \frac{1}{2}\Phi_{nn} \right) + \Gamma_n A_n \frac{\Phi_n - \Phi_p}{dy} \quad (22)$$

$$F_s = u_s A_s \left(\frac{3}{2}\Phi_p - \frac{1}{2}\Phi_n \right) + \Gamma_s A_s \frac{\Phi_p - \Phi_s}{dy} \quad (23)$$

By continuity, the sum of the fluxes through cell P equals 0, and the weighting factors are obtained:

$$a_w = \frac{3}{2}u_w A_w + \Gamma_w \frac{A_w}{dx} + \frac{1}{2}u_e A_e \quad (24)$$

$$a_{ww} = -\frac{1}{2}u_w A_w \quad (25)$$

$$a_e = \Gamma_e \frac{A_e}{dx} \quad (26)$$

$$a_{ee} = 0 \quad (27)$$

$$a_n = \frac{3}{2}u_n A_n + \Gamma_n \frac{A_n}{dy} + \frac{1}{2}u_s A_s \quad (28)$$

$$a_{nn} = -\frac{1}{2}u_n A_n \quad (29)$$

$$a_s = \Gamma_s \frac{A_s}{dy} \quad (30)$$

$$a_{ss} = 0 \quad (31)$$

For the SOU scheme, Equation 18 then becomes:

$$\Phi_p = \frac{a_w \Phi_w + a_e \Phi_e + a_n \Phi_n + a_s \Phi_s + a_{ww} \Phi_{ww} + a_{nn} \Phi_{nn}}{a_p} \quad (32)$$

The same principles applies for a three-dimensional situation. When extending from 2D to 3D the terms for top and bottom is added, resulting in four extra coefficients a_t , a_{tt} , a_b and a_{bb} for the SOU scheme (Olsen, 2017).

The First Order Upwind scheme provides better convergence than the Second Order Upwind scheme. However, more accurate results are obtained with second order discretization, especially for triangular and tetrahedral meshes where the flow is not aligned with the mesh.

3.4.1 The SIMPLEC algorithm

The SIMPLE (“Semi-Implicit Method for Pressure Linked Equations”) algorithm was originally developed by Spalding and Patankar at Imperial College, London, in the early 1970s (Patankar, 1980). It is a widely used numerical procedure for the calculation of the unknown pressure field. The aim is to improve the guessed pressure field through an iterative process such that the velocity field satisfies the continuity equation. The basic

assumption employed in the SIMPLE algorithm is that the flow variables can be expressed as:

$$p = p^* + p' \quad (33)$$

$$u = u^* + u' \quad (34)$$

Where p is the pressure and u is the velocity. The index $*$ is used for the initially calculated variables that do not satisfy continuity, and the corrected variables are denoted with an index $'$. The index k denotes the velocity direction.

The calculation process is initiated by guessing a pressure field p^* . Given the guessed values for the pressure, a discretized version of the Navier-Stokes equations is solved to yield velocity components u_k^* as follows (Versteeg and Malalasekera, 2007):

$$a_p u_{k,p}^* = \sum_{nb} a_{nb} u_{k,nb}^* + B_{u_k} - A_k \frac{\partial p^*}{\partial \xi} \quad (35)$$

where a is the sum of the weighting factors, A_k is the surface area of the cell in direction k and ξ is the index for the grid. The value B contains the rest of the terms from the discretization. By subtraction of Equation 35 from the discretized version of the Navier-Stokes equations based on the corrected variables, the following equation emerges (Olsen, 2017):

$$a_p u_{k,p} - a_p u_{k,p}^* = \sum_{nb} a_{nb} u_{k,nb} - \sum_{nb} a_{nb} u_{k,nb}^* - \left(A_k \frac{\partial p}{\partial \xi} - A_k \frac{\partial p^*}{\partial \xi} \right) \quad (36)$$

Using the correction equations 33 and 34, this equation may be rewritten as:

$$a_p u'_{k,p} = \sum_{nb} a_{nb} u'_{k,nb} - A_k \frac{\partial p'}{\partial \xi} \quad (37)$$

In the SIMPLE method, the first term on the right hand side of Equation 37 is omitted to simplify the velocity correction equations. The following equation is obtained:

$$u'_{k,p} = \frac{A_k}{a_p} \frac{\partial p'}{\partial \xi} \quad (38)$$

For the SIMPLEC method, which is used in Ansys Fluent, a more correct formula for the velocity correction is used. The velocity correction used in the SIMPLEC method is given in Equation 39. This results in a larger correction, and the solution will move more rapid towards convergence compared to SIMLPE (Olsen, 2017).

$$u'_{k,p} = \frac{A_k}{(a_p - \sum_{nb} a_{nb})} \frac{\partial p'}{\partial \xi} \quad (39)$$

Equation 39 gives the velocity corrections once the pressure corrections are known. To obtain the pressure corrections, the continuity equation is used for the velocity correction for a cell. Substitution of the corrected velocities into the continuity equation gives the equation for the pressure correction p' (Olsen, 2017):

$$a_p p'_p = \sum_{nb} a_{nb} p'_{nb} + b \quad (40)$$

Where the source term b is the continuity defect arising from the incorrect velocity field u^* . The correct pressure field is obtained and the continuity equation is satisfied when the pressure correction from Equation 40 is added to the pressure. To summarize, the iterative procedure using the SIMPLEC algorithm is listed in the following (Patankar, 1980):

1. Guess the pressure field p^*
2. Solve the discretized momentum Equations 35 to obtain u^*
3. Solve Equation 40 to find the pressure correction p'

4. Correct the pressure p by adding p' to the guessed pressure field p^*
5. Correct the velocities u^* with u' using Equation 34
6. Treat the corrected pressure p as a new guessed pressure p^* and return to step 2. The procedure is repeated until a converged solution is obtained.

3.5 Turbulence modelling

Flow in a conduit can be classified into the two main categories laminar flow and turbulent flow, and also a transition between them. Laminar flow occurs at relatively low flow velocity, and is envisaged as a layered flow through a smooth path with no disruption between adjacent layers. When the flow velocity exceeds a certain limiting value, the laminar flow becomes unstable (Dey, 2014). Turbulent flow is characterized by flow through an irregular and chaotic path that comprises eddies, swirls and flow instabilities. Figure 15 illustrates the difference between laminar, transitional and turbulent flow in a pipe.

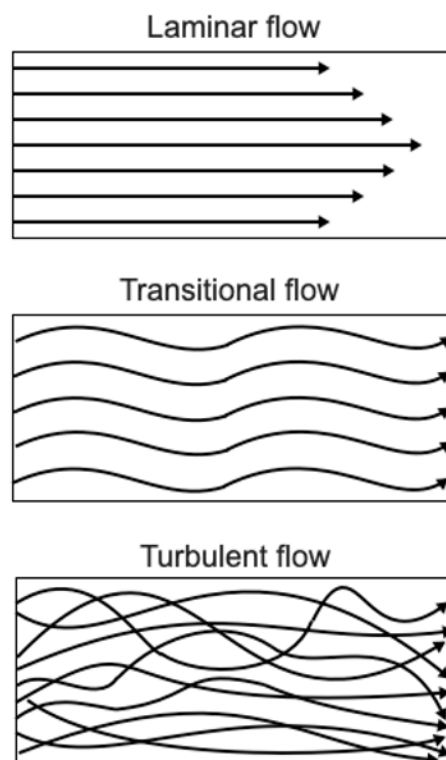


Figure 15: Laminar, transitional and turbulent flow.

The Reynolds number is used to determine whether the flow is laminar or turbulent. In

the late nineteenth century, Osborne Reynolds performed experiments injecting dye into a pipe and observed how the dye followed a straight line for low velocities (laminar flow), and got mixed with the water for higher velocities (turbulent flow). The Reynolds number is a dimensionless value given by the ratio of internal forces to viscous forces:

$$Re = \frac{\text{inertial force}}{\text{viscous force}} = \frac{\rho u d}{\mu} = \frac{u d}{\nu} \quad (41)$$

where Re is the Reynolds number [-], ρ is the density of water [kg/m^3], u is the flow velocity [m/s], d is the conduit diameter [m], μ is the dynamic viscosity of water [Ns/m^2] and ν is the kinematic viscosity of water [m^2/s]. If the viscous forces are dominant, corresponding to low Reynolds number, the flow is laminar. On the contrary, if the inertial forces are dominant, the flow is turbulent with rapid change of velocity in time and space. A classification of flow in a closed conduit based on the Reynolds number is given in Table 1 (Dey, 2014).

Table 1: Flow types according to Reynolds number.

Flow type	Reynolds number
Laminar flow	$Re \leq 2300$
Transitional flow	$2300 \leq Re \leq 4000$
Turbulent flow	$Re \geq 4000$

Turbulence models are more simplified descriptions of the turbulence that are less computational demanding, but also reduces the accuracy. Several numerical methods exist for the calculation of turbulent flows, among these Direct Numerical Simulations (DNS). DNS solves the Navier-Stokes equations directly without any turbulence model. It can give the most accurate results, but the computational requirements are very high and rapidly increasing with increasing Reynolds number. The application of DNS is therefore limited to flows with low Reynolds number and small computational domains. Another method is the Large Eddy Simulation (LES). The idea behind LES is to reduce the computational cost by ignoring the eddies smaller than a certain size by a spatial filtering

operation of the unsteady Navier-Stokes equations (Versteeg and Malalasekera, 2007). The large-scale eddies are directly simulated, while a sub-grid scale model is applied to solve for the small-scale eddies. LES solves unsteady flow equations, resulting in large computing resources in terms of storage and volume.

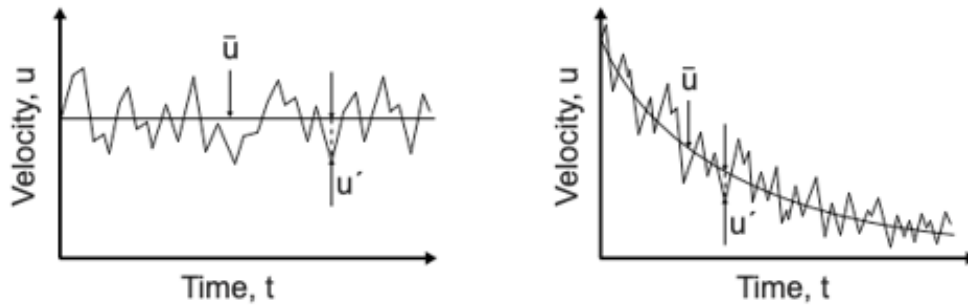


Figure 16: Time averaging for steady (left) and unsteady turbulent flow (right).

The Reynolds-Averaged Navier-Stokes equations (RANS) is a common approach with modest computing resources required for reasonably accurate flow computations. The method focuses on the development of the turbulence and the average effects rather than resolving the details of the turbulent fluctuations, meaning that the pressure and velocity are time averaged prior to the application of numerical methods (Versteeg and Malalasekera, 2007). The time averaged velocity is illustrated in Figure 16, resulting in the expression $u = \bar{u} + u'$, where u' is the fluctuating velocity component. The pressure is time averaged in the same way as the velocity, resulting in the Reynolds-Averaged Navier-Stokes Equations:

$$\rho \frac{\partial \bar{u}_i}{\partial t} + \rho \frac{\partial \bar{u}_i \bar{u}_j}{\partial x_j} = -\frac{\partial \bar{p}}{\partial x_i} + \mu_t \frac{\partial^2 \bar{u}_i}{\partial x_j^2} - \frac{\partial}{\partial x_j} (\rho \overline{u'_i u'_j}) \quad (42)$$

The last term on the right hand side of the RANS equations, called the Reynolds stress term, is obtained from velocity fluctuations and provides additional stresses due to turbulence (Dey, 2014). These terms are modelled with turbulence models. There exists different classes of RANS turbulence models, most known being the k- ϵ model and the Reynolds stress model.

3.5.1 The k- ϵ turbulence model

In this master thesis, the realizable k- ϵ model is applied as turbulence model in Ansys Fluent, and will therefore be further discussed. The k- ϵ model is the most common two-equation model used in CFD. Two separate transport equations (PDEs) are solved for two independent turbulent quantities (Jones and Launder, 1972), allowing to determine the turbulent velocity and length scales. The turbulent kinetic energy, k , and the turbulent dissipation, ϵ are used to define the velocity and length scale.

The standard k- ϵ turbulence model is a practical approach that can be applied to a large number of turbulent flows. It is based on the knowledge of the relevant processes causing changes to k and ϵ to minimize the unknowns (Versteeg and Malalasekera, 2007). The k- ϵ model computes the eddy viscosity as (Olsen, 2017):

$$\mu_t = \rho C_\mu \frac{k^2}{\epsilon} \quad (43)$$

Where k is the turbulent kinetic energy, modelled as:

$$\frac{\partial}{\partial t}(\rho k) + \frac{\partial}{\partial x_i}(\rho k u_i) = \frac{\partial}{\partial x_j} \left(\frac{\mu_t}{\sigma_k} \frac{\partial k}{\partial x_j} \right) + P_k - \rho \epsilon \quad (44)$$

$$P_k = \mu_t \frac{\partial u_j}{\partial x_i} \left(\frac{\partial u_j}{\partial x_i} + \frac{\partial u_i}{\partial x_j} \right) \quad (45)$$

where P_k is the production of turbulence, given by Equation 45. The dissipation of k is denoted ϵ and modelled as (Olsen, 2017):

$$\frac{\partial}{\partial t}(\rho \epsilon) + \frac{\partial}{\partial x_i}(\rho \epsilon u_i) = \frac{\partial}{\partial x_j} \left(\frac{\mu_t}{\sigma_\epsilon} \frac{\partial \epsilon}{\partial x_j} \right) + C_{1\epsilon} \frac{\epsilon}{k} P_k - \rho C_{2\epsilon} \frac{\epsilon^2}{k} \quad (46)$$

The five empirical constants in the k- ϵ model are obtained experimentally by comprehensive data fitting for a wide range of turbulent flows, and have the following standard

values (Versteeg and Malalasekera, 2007):

Table 2: Model constants in the k- ϵ turbulence model.

C_{μ}	0.09
σ_k	1.00
σ_{ϵ}	1.30
$C_{1\epsilon}$	1.44
$C_{2\epsilon}$	1.92

The constants σ_k and σ_{ϵ} in Equation 44 and 46 represents the diffusivities of k and ϵ to the eddy viscosity, respectively.

The standard, the RNG and the realizable model are three variants within the k- ϵ model, all of similar form with transport equations for k and ϵ . The realizable k- ϵ model have shown improved performance over the standard k- ϵ model for flows involving rotation, separation and recirculation (Ansys Fluent). The model differs from the standard k- ϵ model in two ways. Firstly, the realizable k- ϵ model contains a new formulation for the turbulent viscosity by making C_{μ} a variable instead of a constant, hence “realizable”. Secondly, a new model equation for the dissipation, ϵ , derived from an exact equation of the mean-square velocity fluctuation.

3.6 Graphic techniques used in CFD

Computer graphics and computational flow visualization are means to display results of a CFD calculation. Some essential graphic techniques frequently used for the presentation of CFD data are discussed in the following (Anderson, 1995).

- *X-Y plots*: an X-Y plot is the simplest technique for graphical presentation of CFD results. They represent the variation of one dependent variable against another independent variable on a two-dimensional graph. Such plots are the most precise

qualitative way for numerical data presentation in a graph. A disadvantage is that X-Y plots do not illustrate the global nature of a set of CFD results in one view.

- *Contour plots*: contour plots are one of the most commonly used methods for graphic representation of data in CFD. In contrast to X-Y plots, contour plots provide a global description of the fluid flow in one single view. A contour line is a curve along which some property is constant in space. The contours are plotted such that the difference between the numerical value of the dependent variable from one contour line to an adjacent contour line is held constant. If the dependent variable is slowly changing in space, the adjacent contour lines are widely spread together. In the opposite, contour lines are closely spaced if the dependent variable is rapidly changing in space. A contour plot can also be presented as a flooded contour, meaning that the regions between the contour lines are filled with color. The color shading intensity denotes the value of the flow field property.
- *Vector plots*: in a vector plot, a vector quantity is displayed at discrete grid points. The orientation and size indicates the direction and magnitude, respectively. Streamlines are lines instantaneously tangent to the mean velocity vector. They illustrate imaginary particles passing through the flow and plots of streamlines can be used as a tool to visualize the flow pattern.

3.7 Error and uncertainty in CFD modelling

CFD modeling of hydraulic problems can provide a significant reduction in computational resources. However, it is important to be aware of the potential errors and uncertainties in order to develop reliability and confidence in CFD simulations. The following definitions of error and uncertainty in CFD modelling are widely accepted (AIAA, 1998):

- *Error*: a recognizable deficiency in a CFD model that is not caused by lack of knowledge.
- *Uncertainty*: a potential deficiency in a CFD model that is caused by lack of knowledge.

A classification of errors and uncertainties in CFD is listed in Table 3 (Versteeg and Malalasekera, 2007).

Table 3: Errors and uncertainties in CFD.

Numerical errors	
Round-off error	The number of significant digits may affect the solution accuracy
Iterative convergence error	The difference between a fully converged solution and the solution at the end of a simulation
Discretization error	Occurs from the approximate representation of flow variables in a discrete domain of space and time
Coding errors	
Programming error	Bugs or mistakes in the software
Usage errors	
Human error	Incorrect use of the software
Input uncertainty	
Domain geometry	The CFD model deviation from the real geometry
Boundary conditions	Incorrect location and type of boundary condition. The accuracy of the assumptions made will affect the calculation result.
Fluid properties	Inaccurate assumption of constant fluid properties, for example density and viscosity.
Physical model uncertainty	
Application of submodels	Choice of submodels for the modelling of complex flow phenomena, such as turbulence
Simplifying assumptions	The accuracy of simplifying assumptions in the modelling process determines the extent of physical model uncertainty

Verification and validation are the two main processes for assessing the accuracy and reliability in computational simulations. The verification involves determining that a model accurately represents the description of the model (Versteeg and Malalasekera, 2007). The validation procedure determines the deviation between the model and the real world, for instance by comparing computational results with experimental data. Thus, the verification and validation processes quantifies the errors and uncertainties, respectively.

4 Numerical modelling with Ansys Fluent

4.1 Ansys Fluent

Ansys Fluent is a commercial computer program for the modelling of flow, turbulence, heat transfer and reactions for industrial applications (Ansys Fluent). Ansys Fluent is a finite volume based solver that can be applied for large models with complex geometries. When the geometry is imported and the mesh is generated, the remaining simulation processes are performed with Ansys Fluent.

Ansys simulations are commonly performed using the Ansys Workbench. Ansys Workbench is a simulation framework that connects the different simulation processes through the project page. An appropriate analysis system for the simulation is selected in the toolbox and introduced into the project schematic by drag-and-drop. In the project schematic, the analysis system is divided into several blocks that represents the different steps in the simulation process. The user works through the system from the top down, and a green check mark appears when a step in the analysis is completed. Figure 17 shows the Ansys Workbench with the toolbox for different simulation systems to the left. In the figure, the analysis system is Ansys Fluent which is fully integrated into the Ansys Workbench. As shown in the project schematic, the system is complete through mesh generation, indicated by the green check mark.

Passing from one simulation step to another is automatically performed by the framework. An advantage of Ansys Workbench is the project update mechanism, meaning that the downstream cells are updated when changes are made in an upstream cell. This mechanism reduces the effort required to apply variations on a completed analysis (Ansys Fluent).

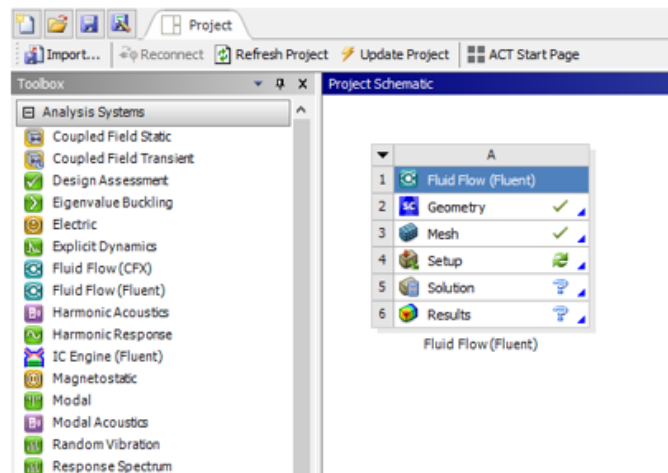


Figure 17: Ansys Workbench.

To perform simulations of Sand trap 3 at Tonstad hydropower plant, the free academic version Ansys Fluent 2019R3 is used. The academic version has some limitations compared to the commercial version, which will be further described in the following sections.

4.2 Creating the geometry

The geometry used for the simulations is created with the 3D modelling software Ansys SpaceClaim. The geometry is based on the construction drawings of Sand trap 3 at Tonstad hydropower plant, provided by Sira-Kvina power company. The drawings are found in Appendix A.

The 1:1 model has the same shape and dimensions as the prototype. The inlet of the model is placed immediately downstream of the surge tank, meaning 2.7 m downstream the gate. The rectangular outlet is created at section 7-7 on drawing 6028^A, that is, right before the pressure shaft cross-section changes to circular. The placement of the inlet and outlet in the model results in a total length of 216.4 m. The different cross-sections are combined using the *Blend* tool in SpaceClaim. The model is shown in two different views in Figure 18. To simplify the simulations, the access tunnel is neglected in the model.

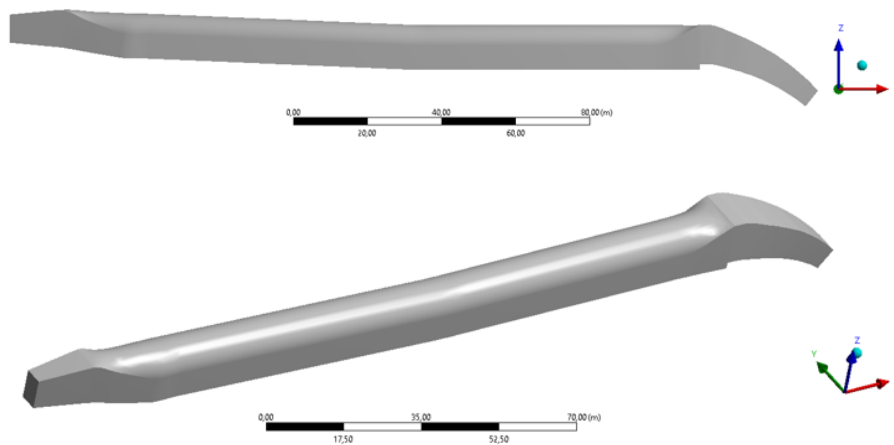


Figure 18: Sand trap model.

For the simulations of the sand trap rebuilt as a closed sand trap, the same model is constructed with horizontal shear plates. At first, a shear plate is placed immediately upstream of the weir, with the top of the shear plate at the same elevation as the top of the weir. Equal shear plates are placed further upstream until they reach the inclined part of the sand trap. The shear plates covers the entire width of the sand trap, and have a thickness of 0.2 m and length of 1.0 m in the x-direction. According to the recommendations, the spacing between them are similar to the length, resulting in 54 shear plates over a length of 107 meters. Figure 19 shows the sand trap constructed with horizontal shear plates.

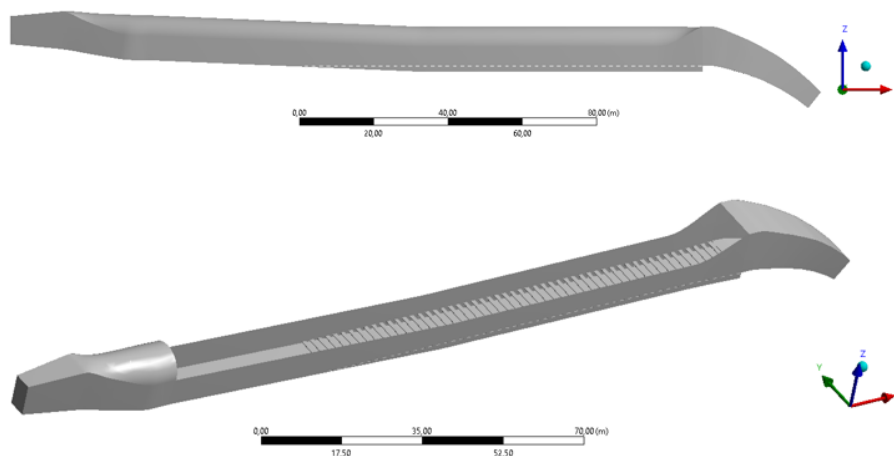


Figure 19: Sand trap model with horizontal shear plates.

The *Volume Extract* tool creates a solid that represents an internal volume of the model. This tool is used to deal with the limitation of 300 faces and 50 bodies in the Ansys academic version.

4.3 Mesh generation

The mesh is generated with the Ansys Meshing software. A symmetry plane that cuts the symmetrical model along the x-axis is applied, not only to save computational time, but also due to the limitation of 512 000 elements for the CFD model with the Ansys academic version. With the symmetry plane, a finer mesh can be applied within the limitation compared to the entire model.

In meshing mode, *Named Selections* are created to be able to set the boundary conditions for the different parts of the model. They are automatically transferred to Ansys Fluent, which assigns the properties that are associated with the given named selection. The named selections for the geometry boundaries includes the inlet, the outlet, the symmetry plane, the walls and the bed. Boundary conditions are not applied for the symmetry plane, but it is defined as a named selection to avoid that Fluent treats the plane as a wall.

The mesh is generated using tetrahedral elements. Refinements are applied on the inlet and outlet to ensure that the flow is appropriately resolved. To cope with the limitation in number of elements, the maximum element size for the mesh is 0.5 m. This results in the following number of nodes and elements for the model:

Table 4: Number of mesh elements and nodes.

Number of nodes	99 444
Number of elements	501 218

In Ansys Meshing, different measures of the grid quality can be displayed. The orthogonal quality, the aspect ratio and skewness are shown in Figure 20-22.

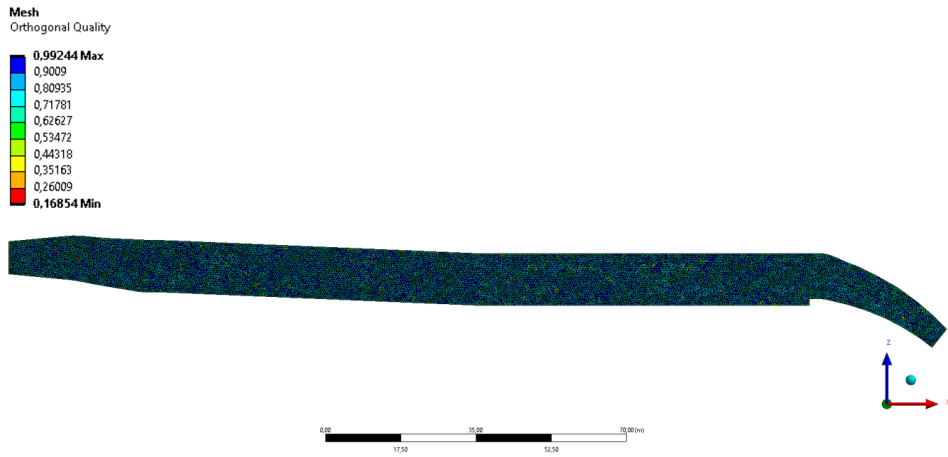


Figure 20: Mesh quality - Orthogonal quality.

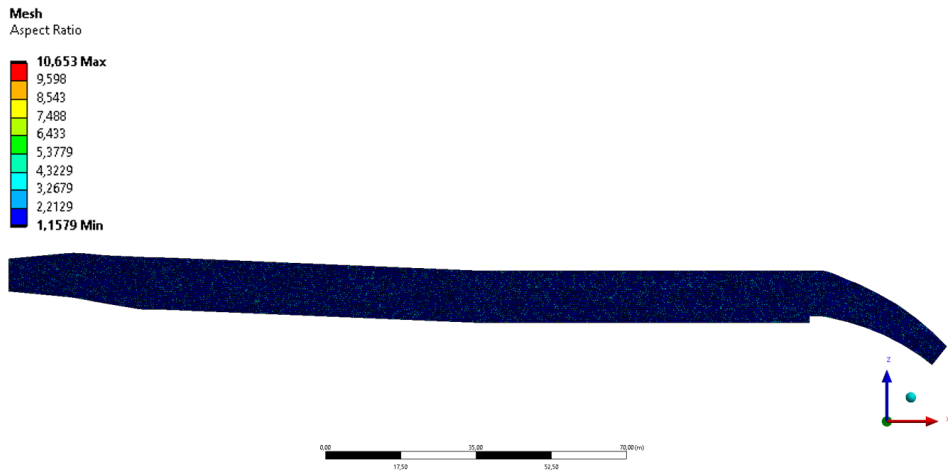


Figure 21: Mesh quality - Aspect ratio.

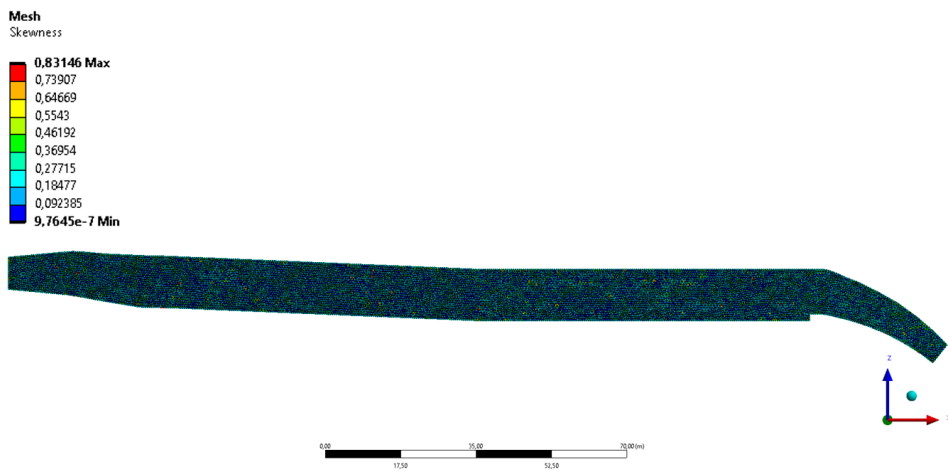


Figure 22: Mesh quality - Skewness.

The legend to the left displays the values with corresponding colors for the different mesh quality measures. Figure 20-22 indicates good mesh quality according to the recommendations described in section 3.2.

4.4 Numerical details and simulation settings

Two different cases are simulated to investigate the effect of installing horizontal shear plates in Sand trap 3 at Tonstad hydropower plant:

1. At first, steady-state k- ϵ Reynolds-Averaged Navier-Stokes (RANS) simulations are run to compare the flow behavior with and without horizontal shear plates.
2. Secondly, transient k- ϵ Reynolds-Averaged Navier-Stokes (RANS) simulations with sediments are run to study the sediment behavior with and without horizontal shear plates.

All of the simulations are carried out using the CFD software Ansys Fluent, with a 3D double precision parallel solver. Double precision means including more decimals in the calculations and thus increasing the solution accuracy. The default fluid simulated in Ansys Fluent is air. A new material is therefore created from the Fluent Database. The *water-liquid* (*h20<l>*) is copied into the material selection tab with the following properties:

$$\text{Density: } \rho = 998.2 \text{ kg/m}^3$$

$$\text{Dynamic viscosity: } \mu = 0.001003 \text{ kg/ms}$$

For the modelling of turbulence, the realizable k- ϵ turbulence model is applied. The SIM-PLEC discretization scheme described in subsection 3.4.1 is used for the pressure-velocity coupling. The momentum, the turbulent kinetic energy and the turbulent dissipation rate are computed using the Second Order Upwind scheme. For the steady state simulations, the convergence criterion is set to 1e-06.

To account for the wall and bed roughness effects, a roughness height and a roughness constant must be specified. A roughness height of zero corresponds to smooth walls. The roughness constant is a value between 0 and 1, depending on the type of the given roughness (Ansys Fluent). The first 13.3 meters downstream the inlet and the part downstream the weir is concrete lined, resulting in a different roughness height compared to the remaining unlined walls. To simplify, it is assumed that the walls for the entire model is unlined rock surface, giving a constant roughness height. The bed in the sand trap is concrete lined. The following values are applied for the walls and the bed (K. Vereide 2020, personal communication, 12 May):

Table 5: Roughness height and roughness constant for the walls and the bed.

	Roughness height	Roughness constant
Walls	0.30	1.00
Bed	0.02	0.50

The walls are modelled with no slip condition, meaning that the velocity at the wall is zero. The simulations are run with the maximum turbine discharge at Tonstad, equal to $80 \text{ m}^3/\text{s}$. By continuity, this results in an inlet velocity of:

$$u_{in} = \frac{Q}{A_{in}} = \frac{80 \frac{\text{m}^3}{\text{s}}}{7.51 \text{ m} \cdot 4.51 \text{ m}} = 2.36 \frac{\text{m}}{\text{s}} \quad (47)$$

where A_{in} is the cross-sectional area of the inlet placed 2.7 m downstream the gate.

Table 6 summarizes the numerical methods and boundary conditions that are used in the simulations.

Table 6: Numerical methods and boundary conditions used in the simulations.

Numerical method	
Solver	Pressure-based
Pressure-velocity coupling	SIMPLEC
Spatial discretization	
Convective terms	Second Order Upwind
Gradient	Least Square Cell based
Boundary conditions	
Inlet	Velocity inlet, $u = 2.36$ m/s
Outlet	Pressure outlet, $p = 0$ Pa
Walls	No-slip

The same numerical methods and boundary conditions are applied for the transient simulations, with a second order implicit transient formulation. An injection can be created when activating the Discrete Phase Model (DPM). Firstly, it is specified that the sediments are to be released from a surface. Releasing sediments from the velocity inlet may cause problems in the simulations. A named selection called sediment inlet is therefore created above the velocity inlet in meshing mode. Releasing the sediments from the top of the model results in conservative predictions regarding the particle settling. Figure 23 shows the sediment inlet, highlighted with a green color.

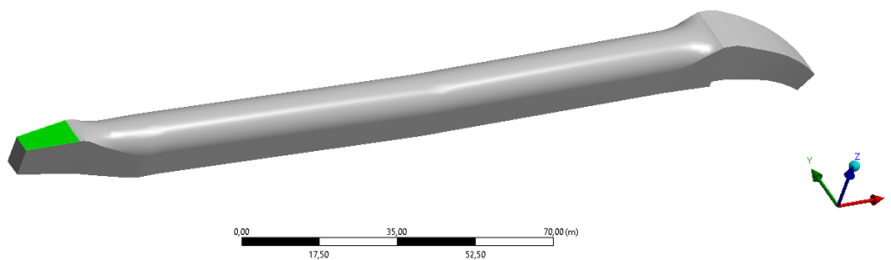


Figure 23: Sediment inlet.

Two different sediment diameters are injected to study how the sediments of different sizes are carried by the water and to check the trap efficiency effect of installing horizontal shear plates. For the first simulations, sediments with a diameter of 1 mm are injected. The total simulation time for these are 200 seconds. Secondly, sediments of 0.3 mm are injected with a total simulation time of 300 seconds to ensure that all particles are either trapped or escaped through the outlet. The details for the sediment injections are given in Table 7.

Table 7: Sediment injection details.

Injection type	Surface: sediment inlet
Particle type	Inert
Diameter distribution	Uniform
Particle density	2650 kg/m ³
X, Y, Z velocity	0 m/s
Start time	0 s
Stop time	20 s
Total flow rate	1 kg/s

Several discrete phase boundary condition types are available in Ansys Fluent. The boundary condition for the sediment inlet and the outlet is *escape*, meaning that the particles vanishes when the they encounters the boundaries. When the particles reaches the bed, the trajectory calculations are terminated and the particles are recorded as *trapped* (Ansys Fluent). The discrete phase boundary conditions for the walls are set to *reflect*, with both the normal and tangential coefficient of restitution assumed a constant value of 0.9 (K. Vereide 2020, personal communication, 12 May).

4.5 Post-processing of the results

The results of the steady state flow simulations are presented with overview plots and detail plots. The detail plots are created to represent readable results of the simulations. Thus, the model is divided into the three following parts:

- Part 1: from the inlet and 35 meters downstream ($x = 0$ to $x = 35$ m)
- Part 2: from 15 meters upstream 15 meters downstream the middle point of the shear plate section ($x = 118$ m to $x = 148$ m)
- Part 3: from 10 meters upstream the weir to 20 meters downstream the weir ($x = 176$ m to $x = 206$ m)

The velocity is presented with vector plots, while the turbulent kinetic energy is presented with contour plots. For the transient simulations with sediments, *Particle Tracks* is defined before running the calculation. This includes points showing the particle trajectories, colored by the particle residence time. When the calculation is complete, a summary of the particle tracks is displayed to obtain the amount of sediments released, escaped and trapped. Thus, the sand trap efficiency can be calculated as described in subsection 2.1.4. A *Solution Animation Playback* can be created to make files showing the particle trajectories during the entire simulation.

5 Results

5.1 Steady state simulations

In this section, the results from the steady state simulations are presented. As described in section 4.4, these simulations consist of one flow simulation without shear plates and one with shear plates. The residuals for the simulation without and with shear plates are shown in Figure 24 and 25, respectively.

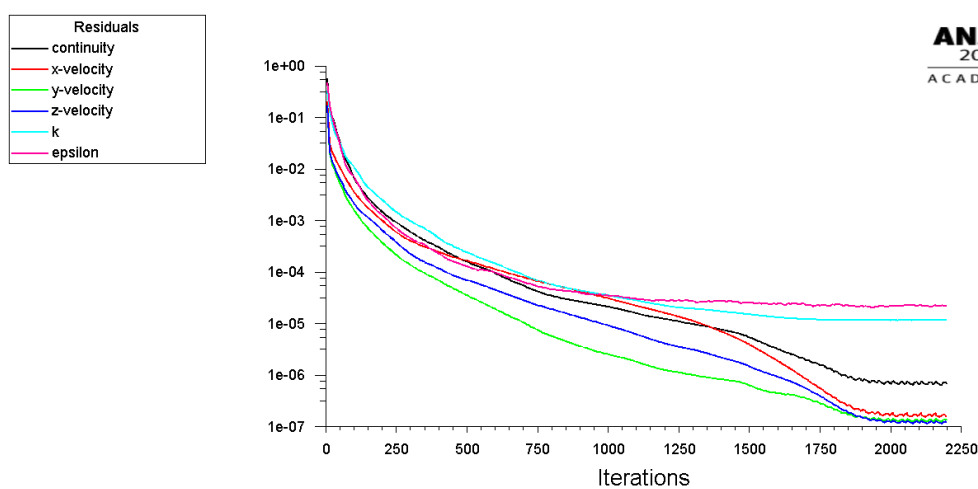


Figure 24: Residuals for the simulation without shear plates.

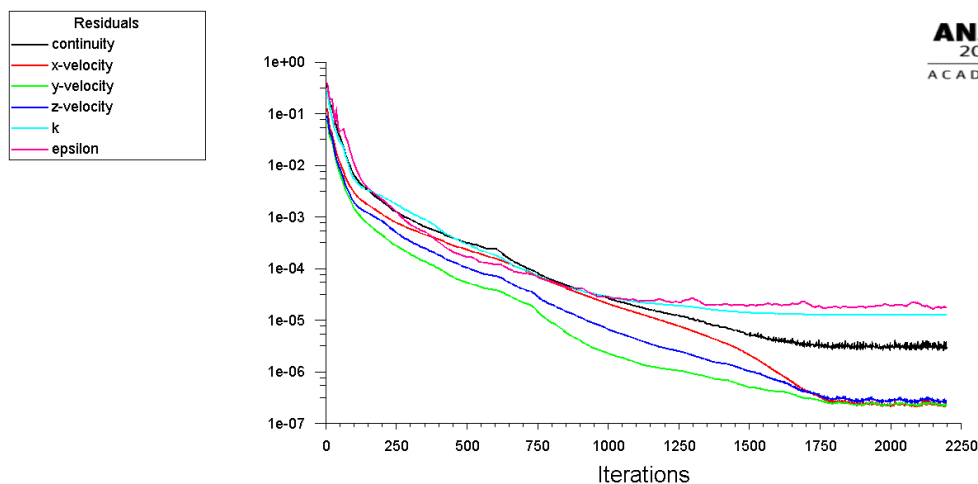


Figure 25: Residuals for the simulation with shear plates.

An overview plot showing the velocity vectors along the bed is given in Figure 26. Figure

27 shows the velocity vectors along the symmetry plane. For both figures, the upper plots is without shear plates while the lower plots presents results with shear plates.

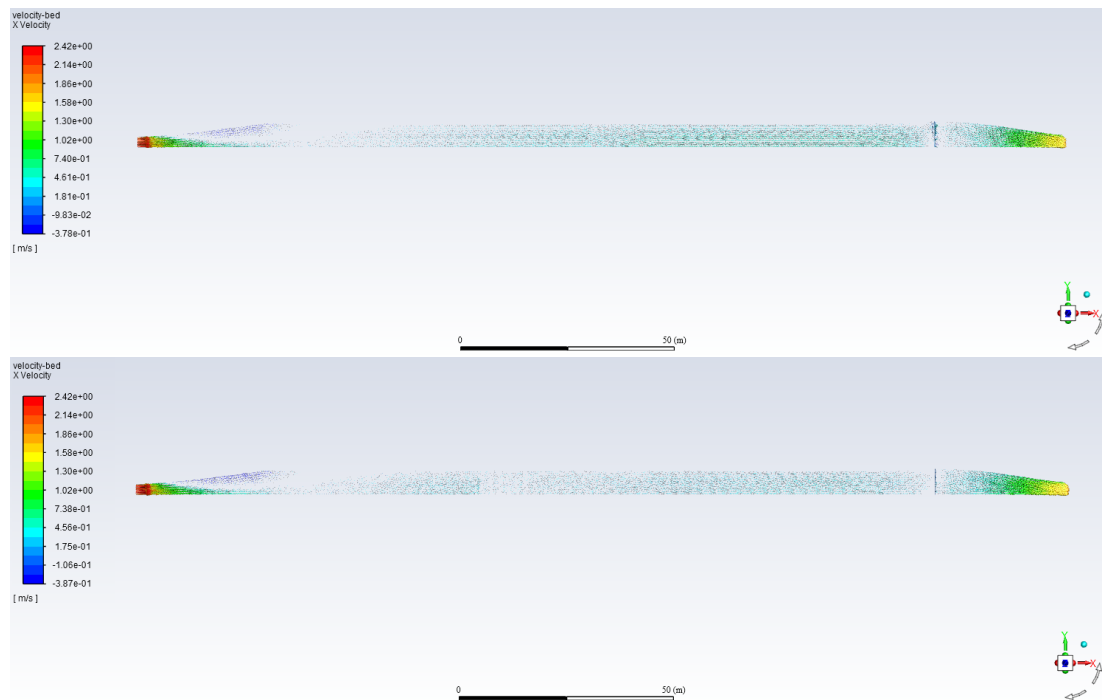


Figure 26: Vector overview plot of the velocity along the bed.

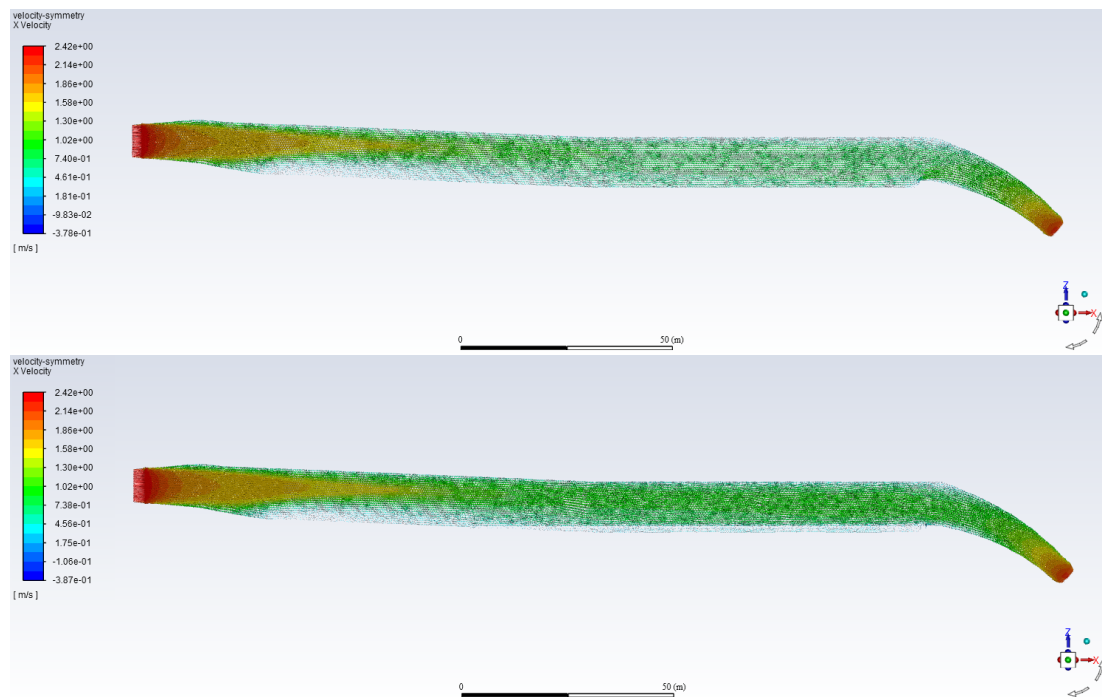


Figure 27: Vector overview plot of the velocity along the symmetry plane.

The overview plots do not provide readable values, they only give an impression of the flow situation. The results are therefore also presented in three sections, as described in section 4.5. The vector plot of the velocity along the bed and the symmetry plane for Part 1 is presented in Figure 28 and Figure 29, respectively. The vector plots for Part 1 are similar for the simulations with and without shear plates.

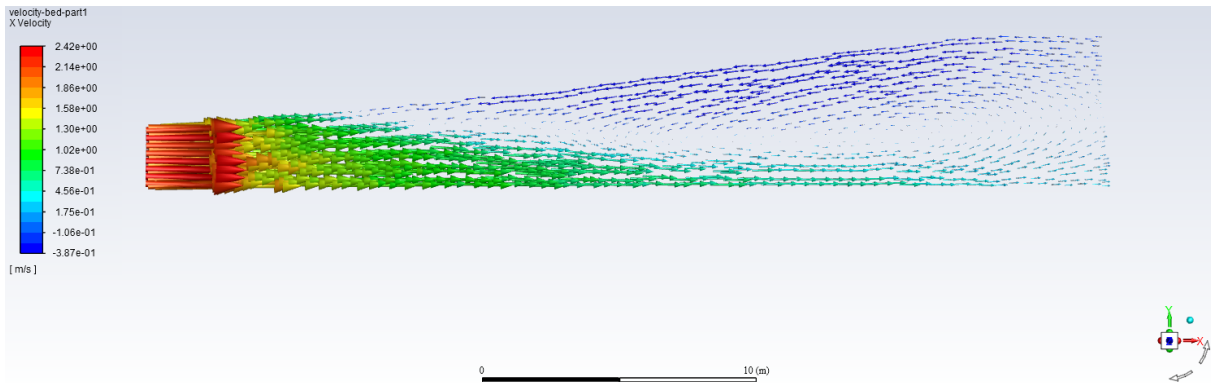


Figure 28: Vector plot of the velocity along Part 1 of the bed.

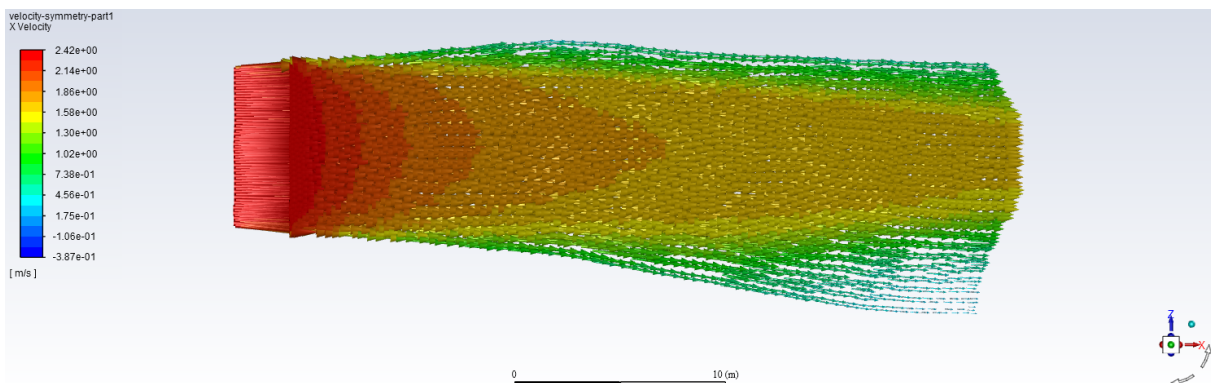


Figure 29: Vector plot of the velocity along Part 1 of the symmetry plane.

Figure 30 - 33 provides a comparison of the velocity with and without shear plates for Part 2 and Part 3. In the figures, the velocity vector plot for the open sand trap is presented above the plots with shear plates installed.

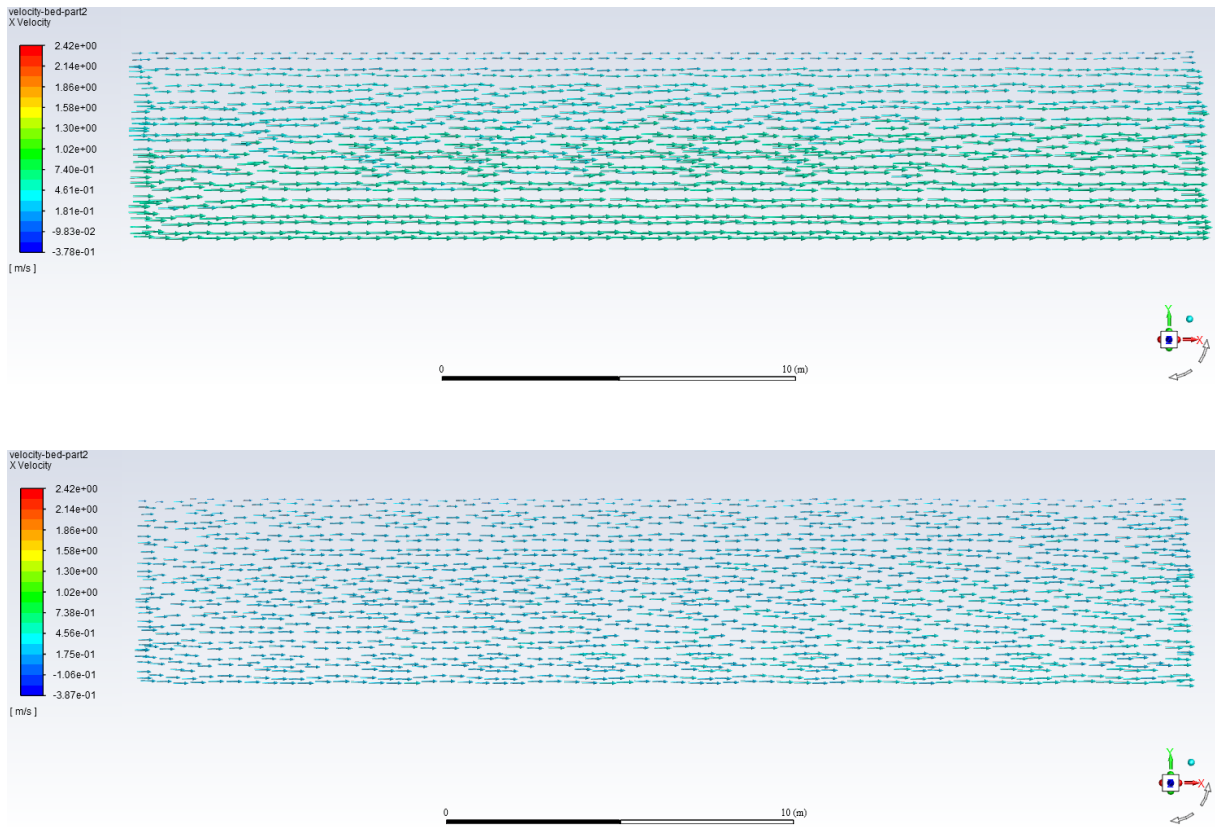
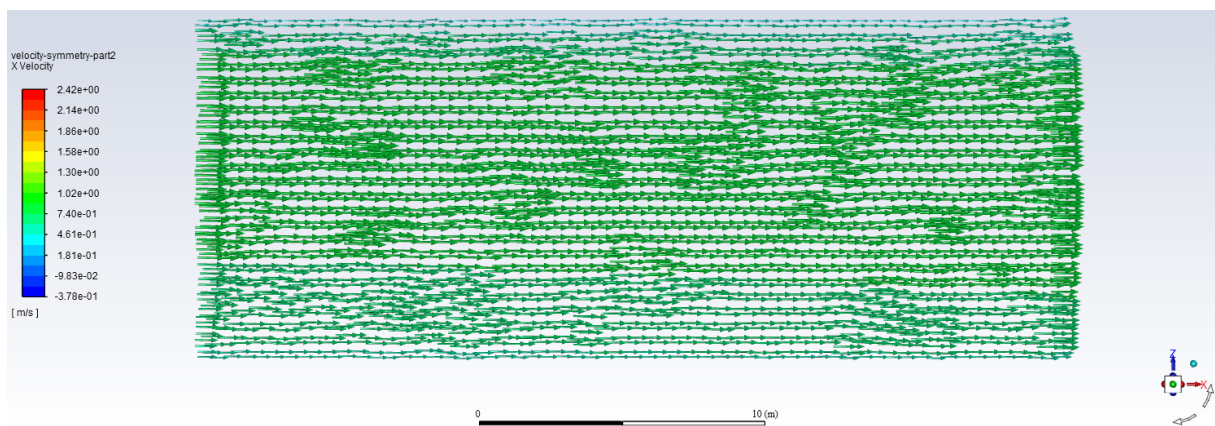


Figure 30: Vector plot of the velocity along Part 2 of the bed.



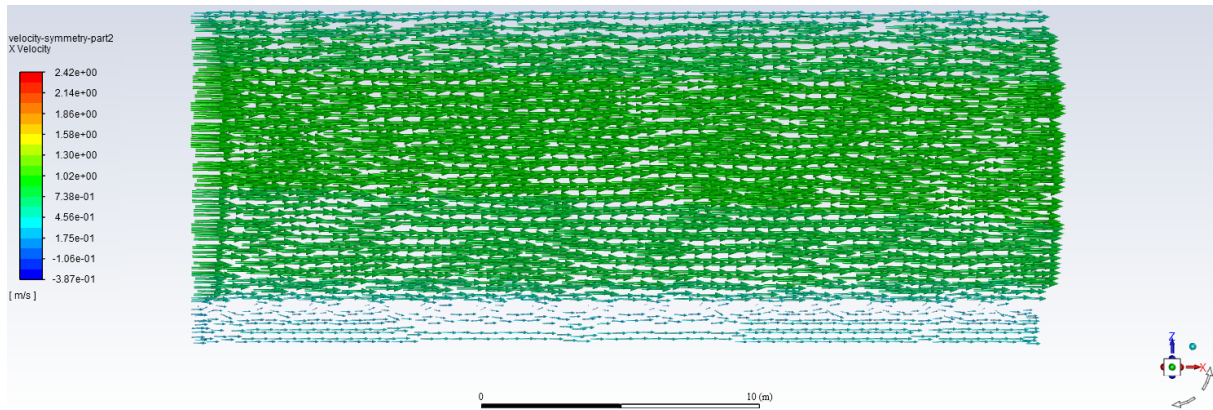


Figure 31: Vector plot of the velocity along Part 2 of the symmetry plane.

Part 3 includes the weir that is located in the downstream end of the sand trap, 188.3 m from the inlet. The shear plates are placed such that the top of the shear plates are at the same elevation as the top of the weir, that is, 1.5 m above the bed.

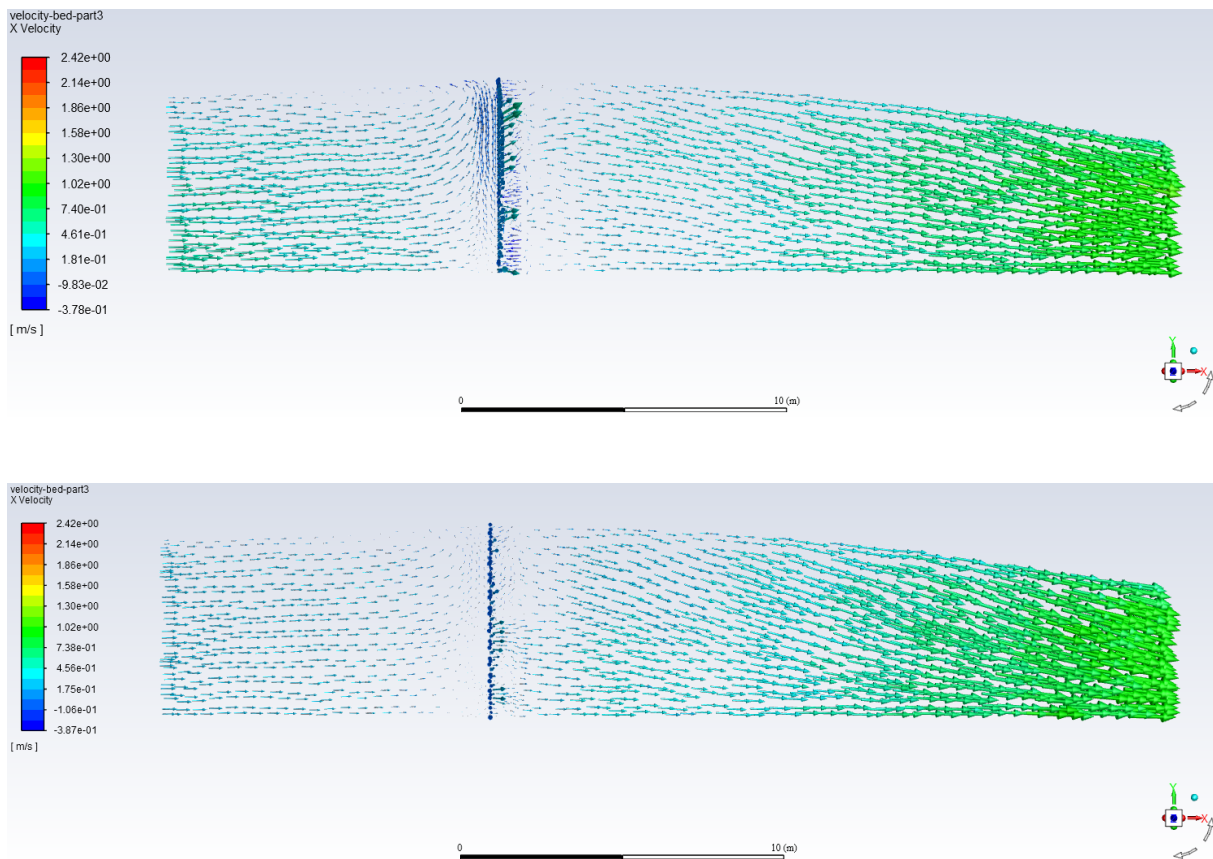


Figure 32: Vector plot of the velocity along Part 3 of the bed.

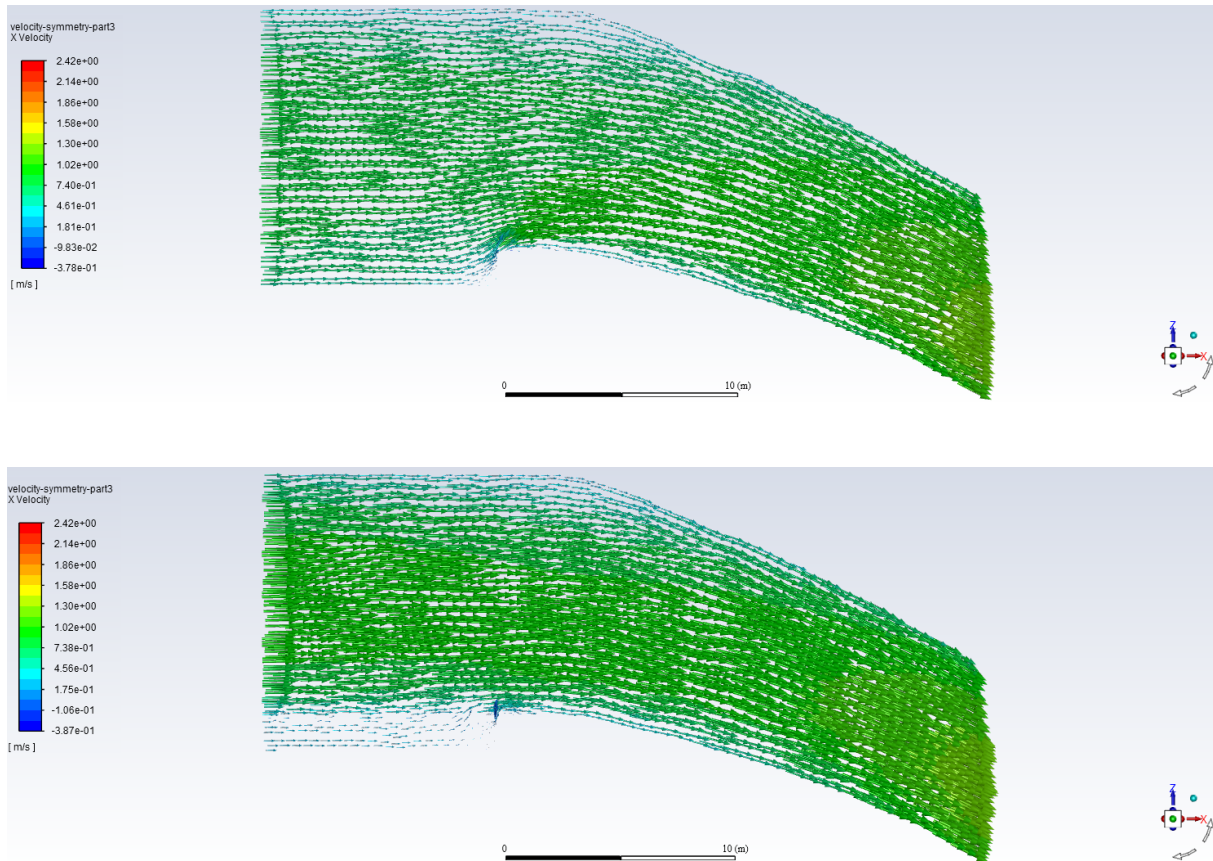
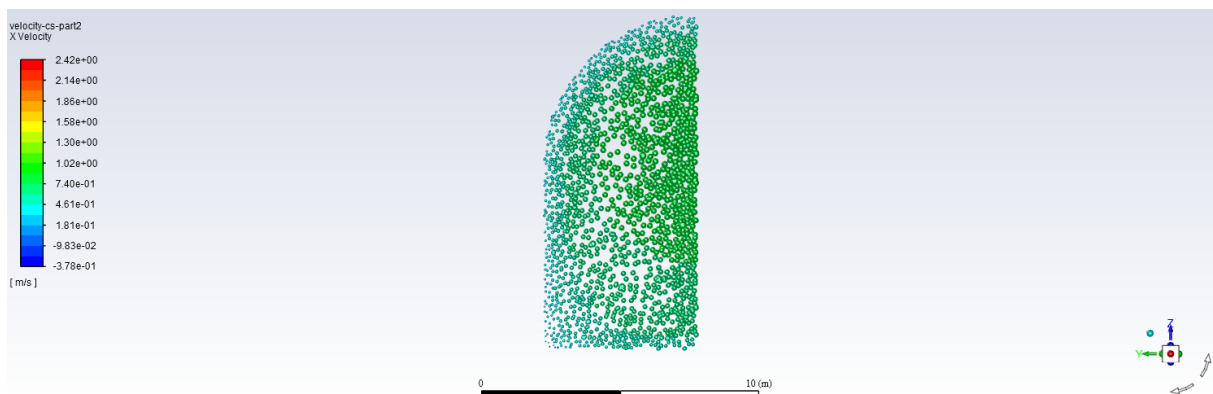


Figure 33: Vector plot of the velocity along Part 3 of the symmetry plane.

In addition, a representation of the velocity in a cross-section immediately upstream the weir is presented in Figure 34 without (upper) and with (lower) shear plates.



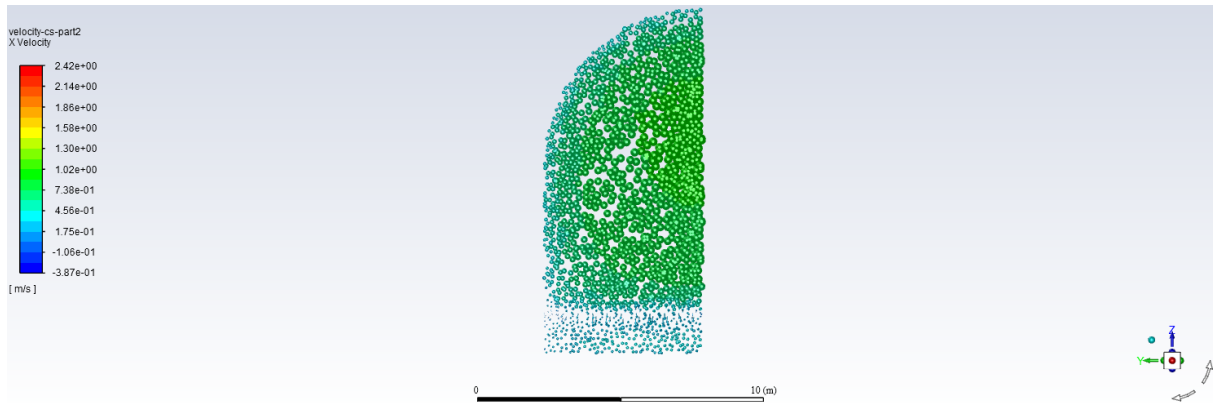


Figure 34: Vector plot of the velocity in a cross-section.

The turbulent kinetic energy is shown in plan view and longitudinal view in Figure 35 and 36, respectively. A clear difference in the turbulent kinetic energy is not observed. However, it can be seen that the values are slightly smaller over the weir with shear plates installed (lower plot) compared to the open sand trap (upper plot).

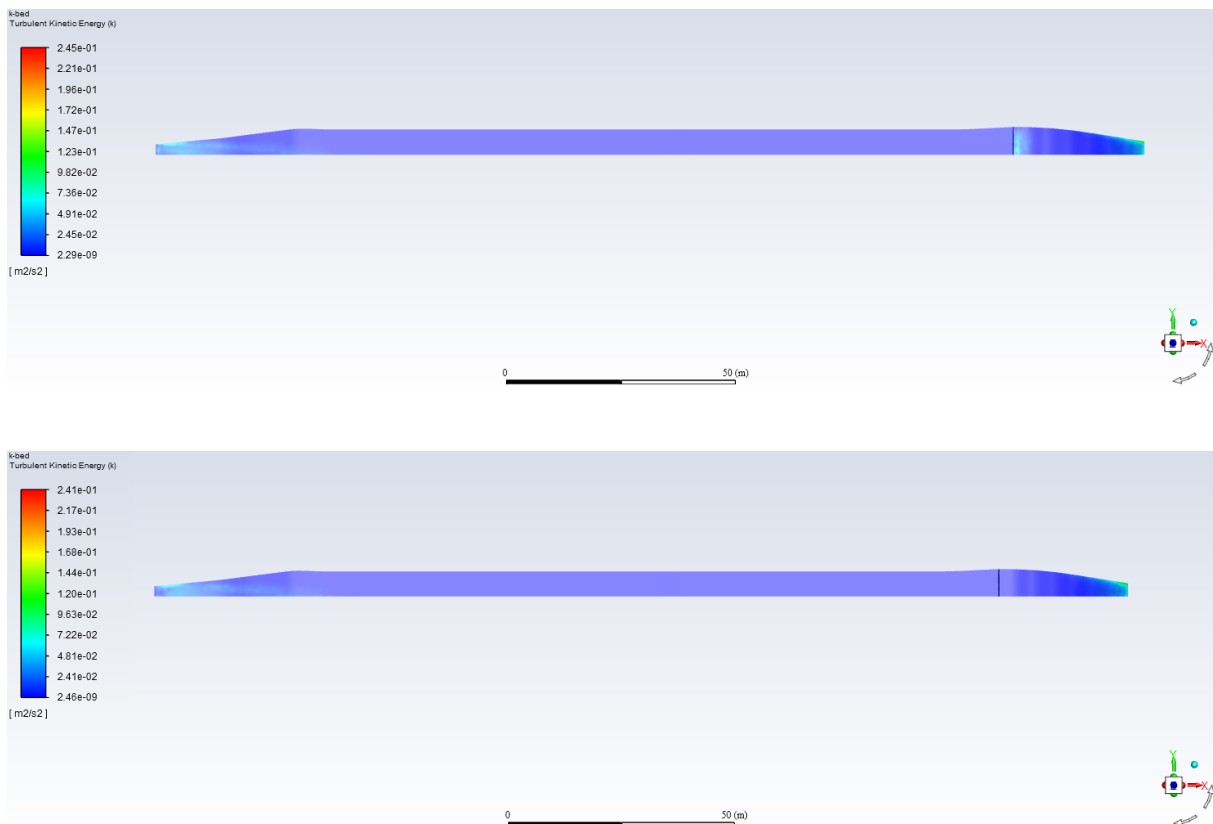


Figure 35: Turbulent kinetic energy along the bed.

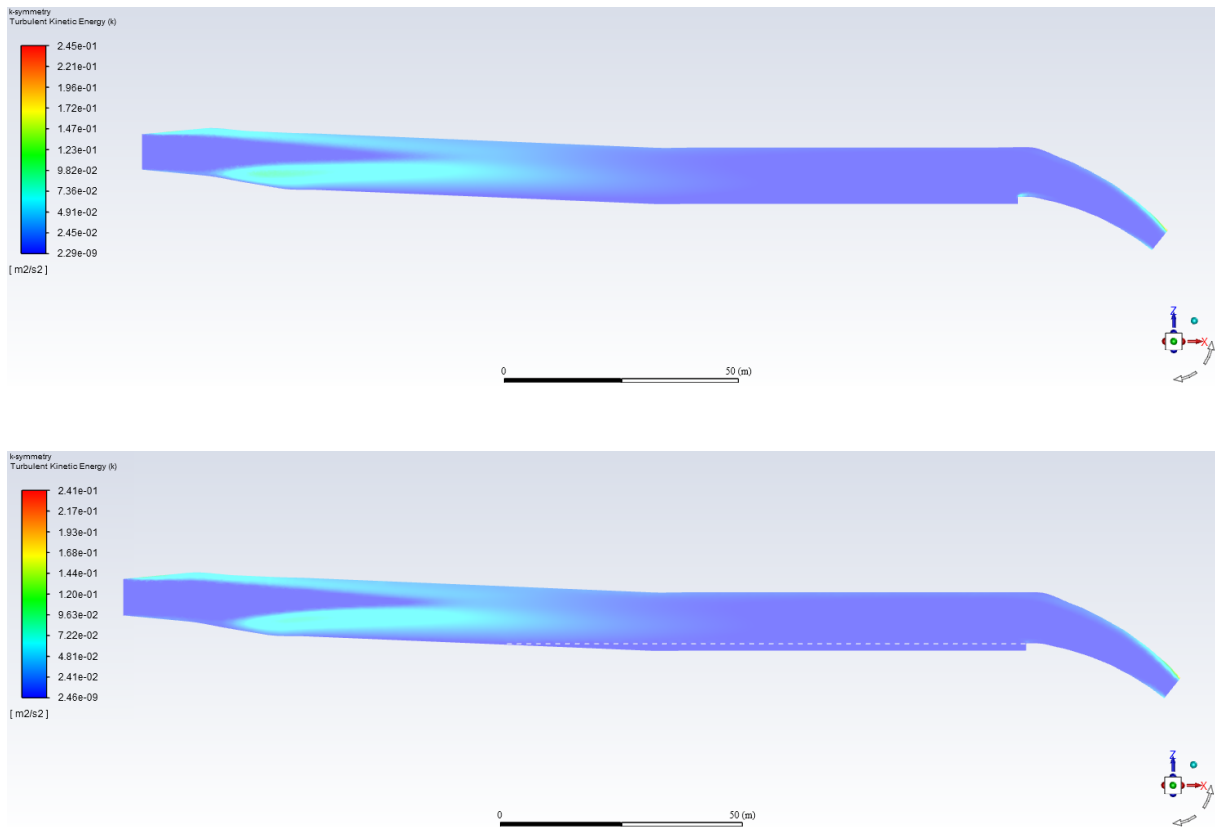


Figure 36: Turbulent kinetic energy along the symmetry plane.

5.2 Simulations with sediments

The results of the transient simulations with sediment injection are given in the following. The particle trajectories are shown for different time steps with 1 mm particles in subsection 5.2.1 and 0.3 mm particles in subsection 5.2.2. The sand trap efficiencies for the different simulations are given in 5.2.3.

5.2.1 Simulations with 1 mm particles

Figure 37-39 shows the particle residence time after 20 s, 50 s and 100, respectively. The results are presented in a longitudinal view (top) and plan view (bottom):

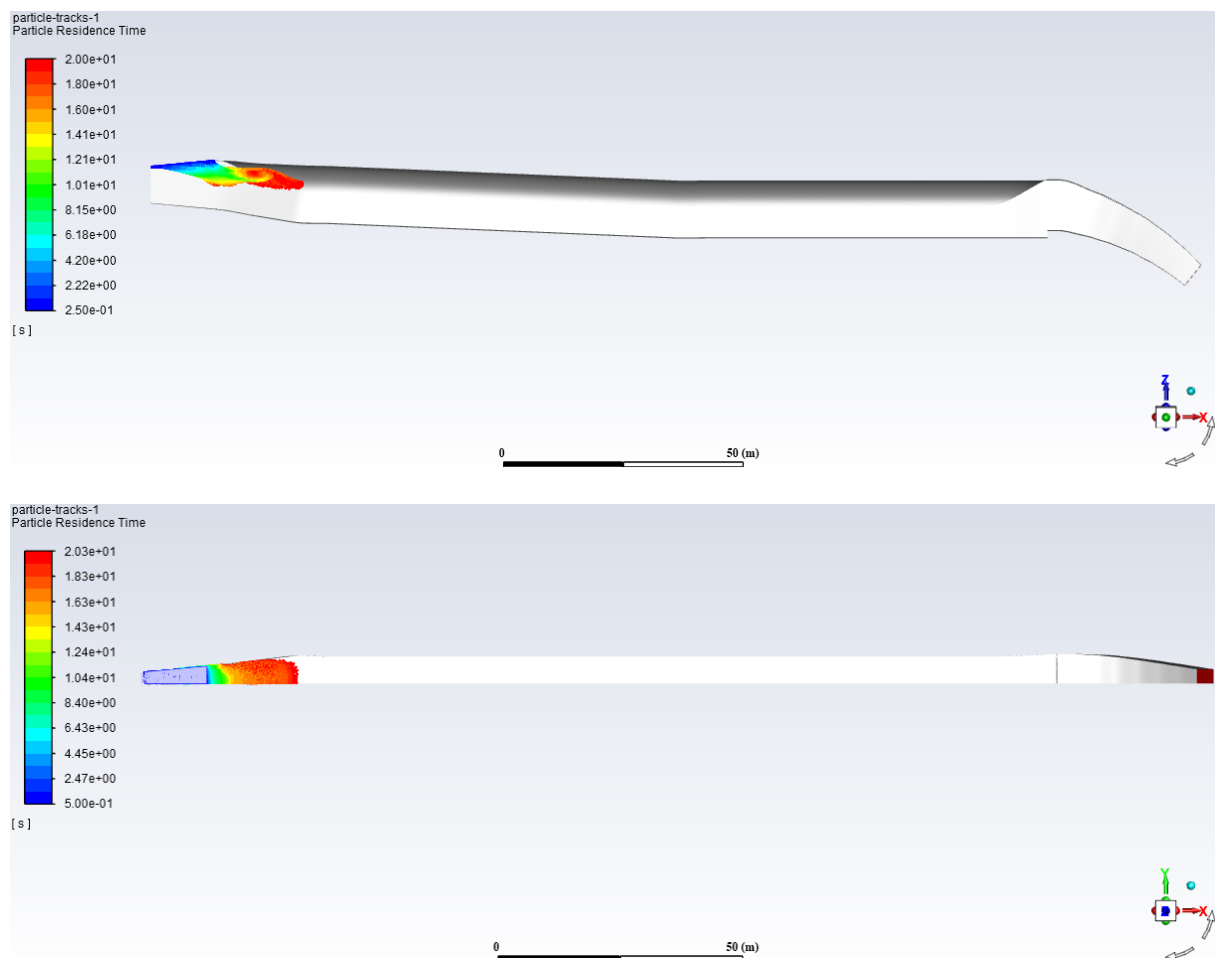


Figure 37: Injection of 1 mm particles after 20 s.

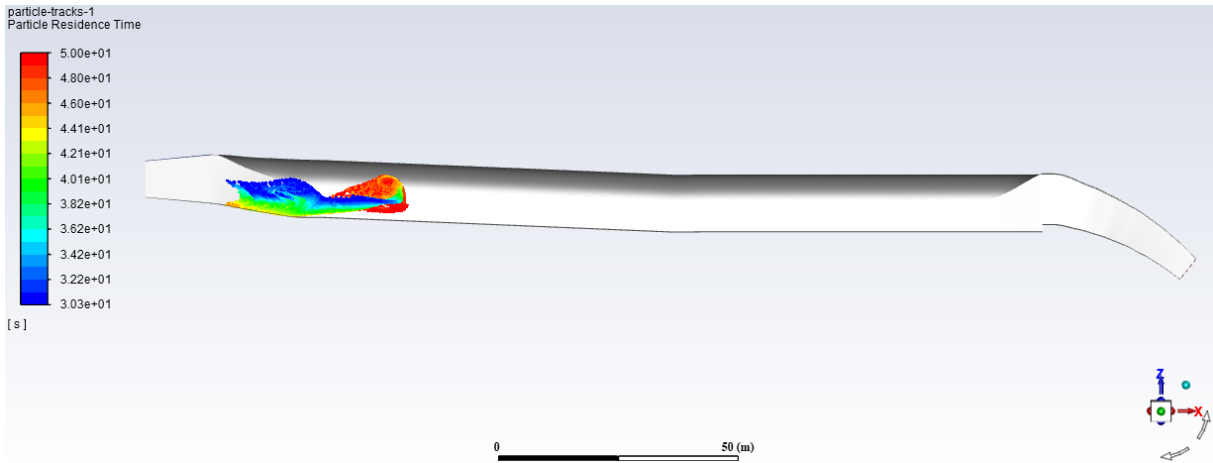
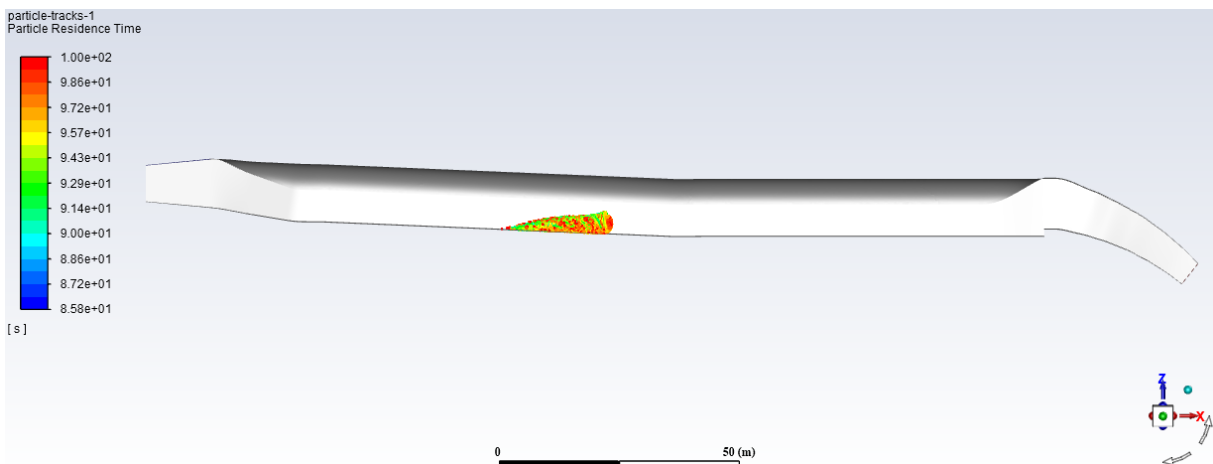


Figure 38: Injection of 1 mm particles - after 50 s.



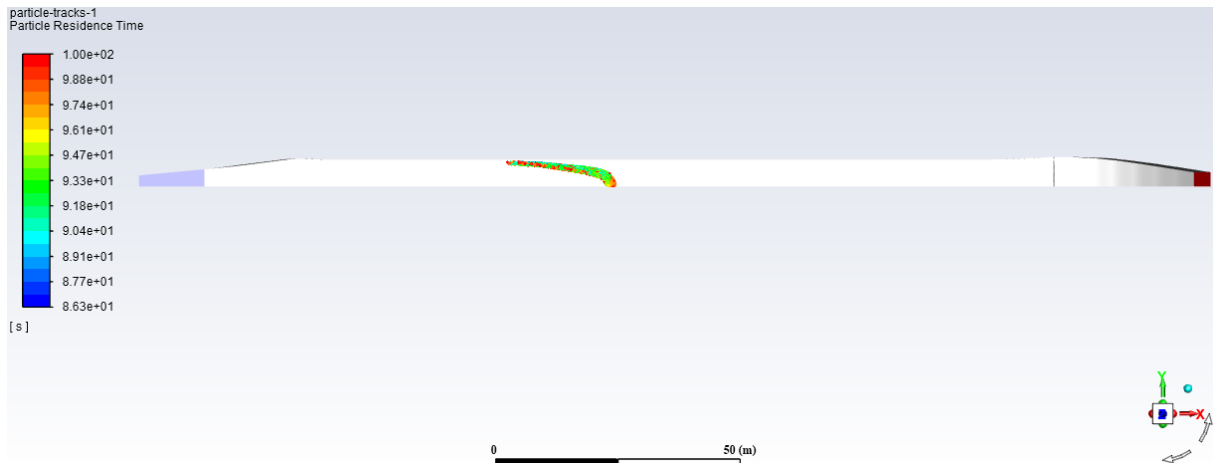


Figure 39: Injection of 1 mm particles - after 100 s.

All of the sediments are trapped at the end of the simulation both with and without horizontal shear plates. Therefore, the path of 1 mm the particles for the case with shear plates are not illustrated. However, it is interesting to check the amount of sediments left in the tunnel at a time step. The following figure shows the amount and placement of the sediments left in the tunnel after 125 s. It can be seen that the 1 mm particles are trapped faster with shear plates installed (lower) than without shear plates (upper):

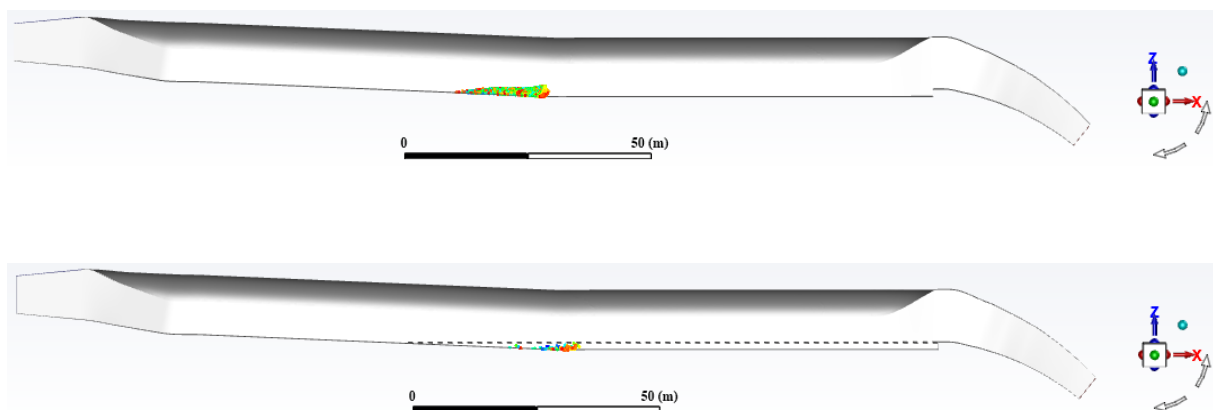


Figure 40: Sediments left in the tunnel after 125 s.

5.2.2 Simulations with 0.3 mm particles

Comparing the flow of the 0.3 mm particles with and without horizontal shear plates is not necessary for the first part of the simulations as the particles have not reached the shear plate region. Instead, the particle trajectories for the open sand trap is presented after 20 s, 50 s and 100 s for comparison with the 1 mm particle trajectories at the same time steps. As in subsection 5.2.1, the results are presented in a longitudinal view (top) and plan view (bottom):

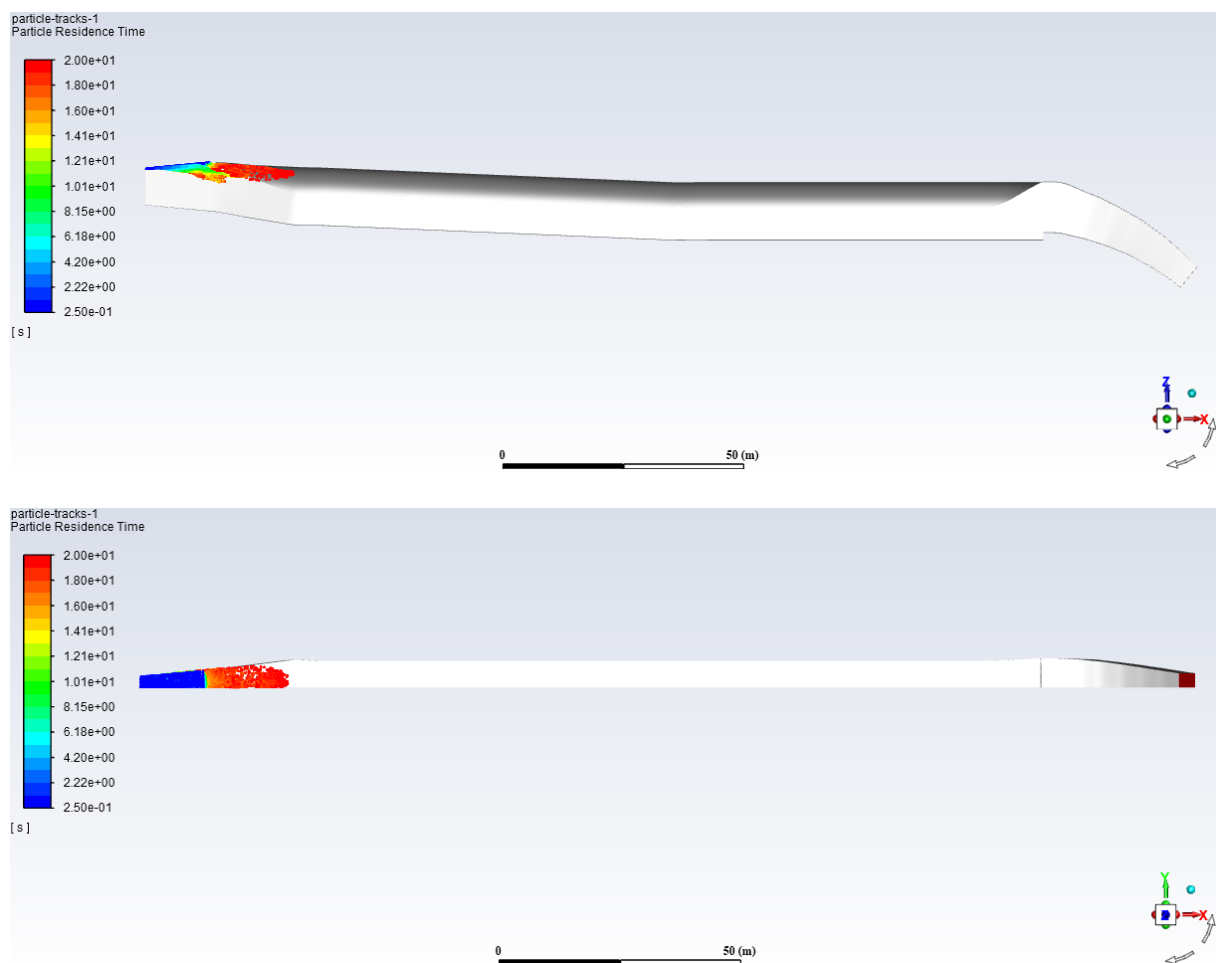


Figure 41: Injection of 0.3 mm particles - after 20 s.

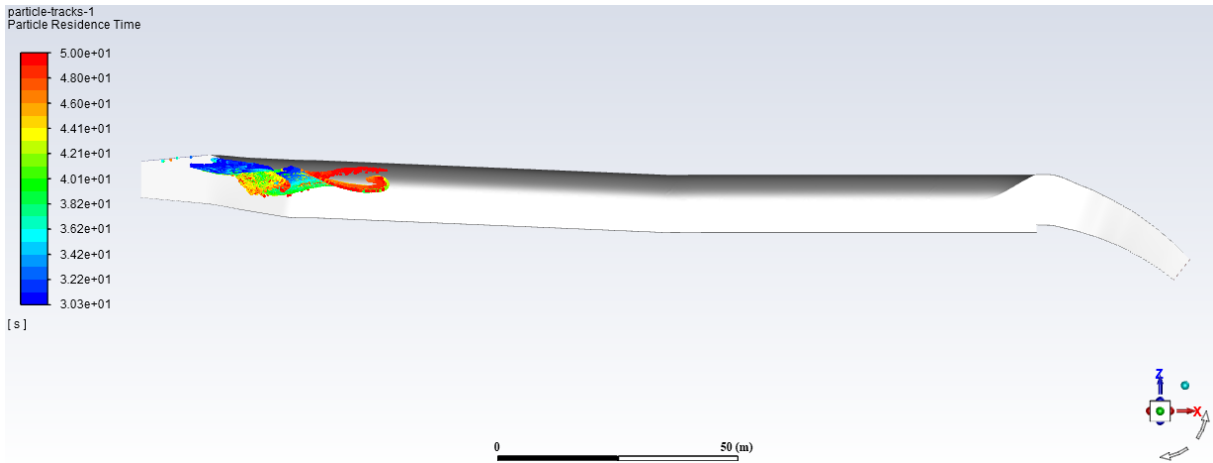
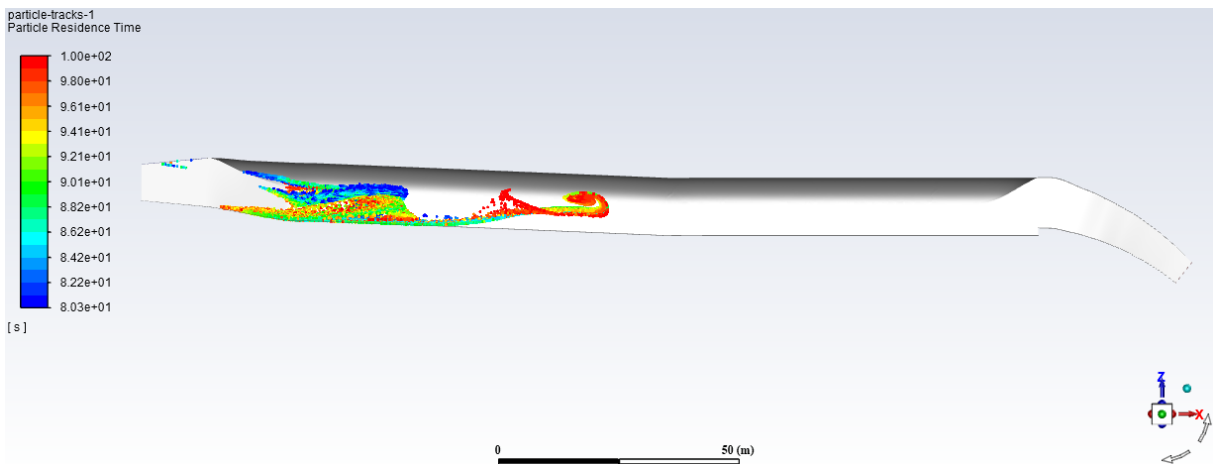


Figure 42: Injection of 0.3 mm particles - after 50 s.



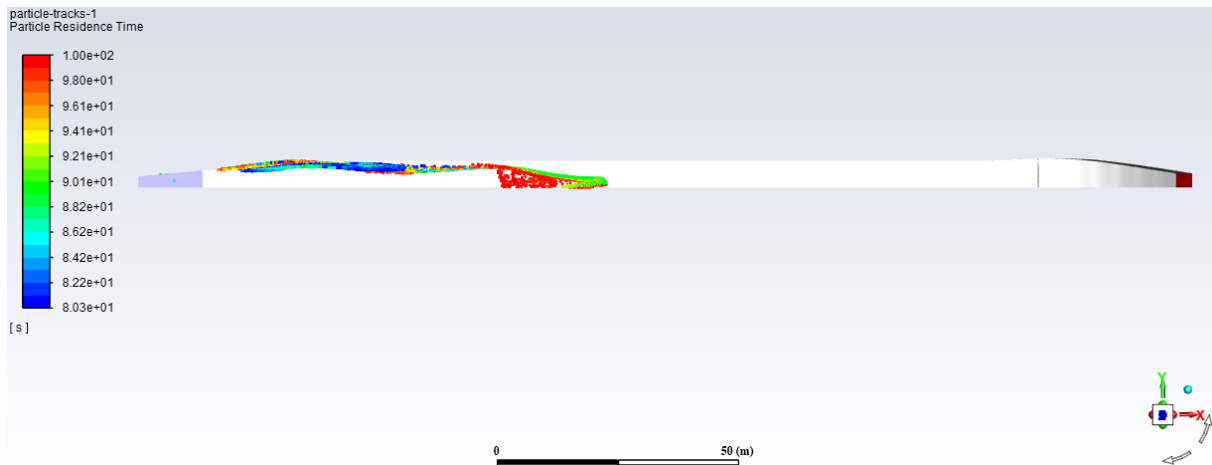
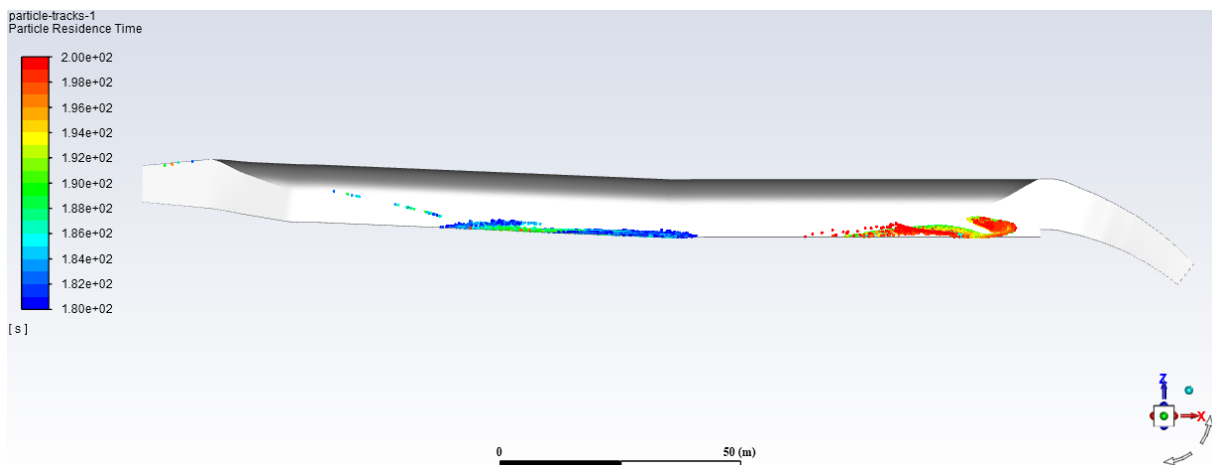


Figure 43: Injection of 0.3 mm particles - after 100 s.

To study the effect of installing horizontal shear plates in the sand trap, the particle residence time is displayed in a longitudinal view after 200 s and 250 s. Figure 44 and 45 shows the particle trajectories without (top) and with (bottom) shear plates 200 s and 250 s after initializing the simulation, respectively.



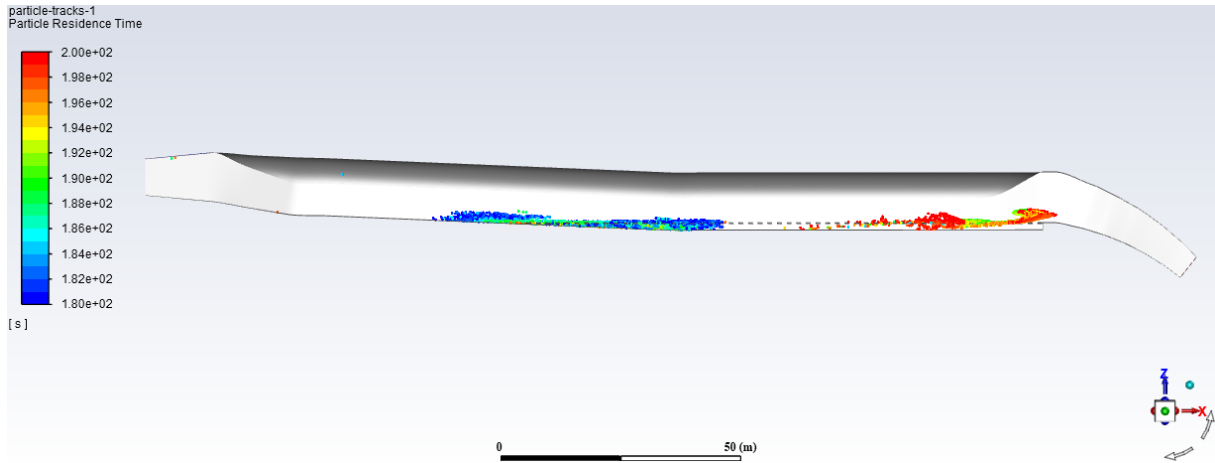


Figure 44: Injection of 0.3 mm particles - after 200 s.

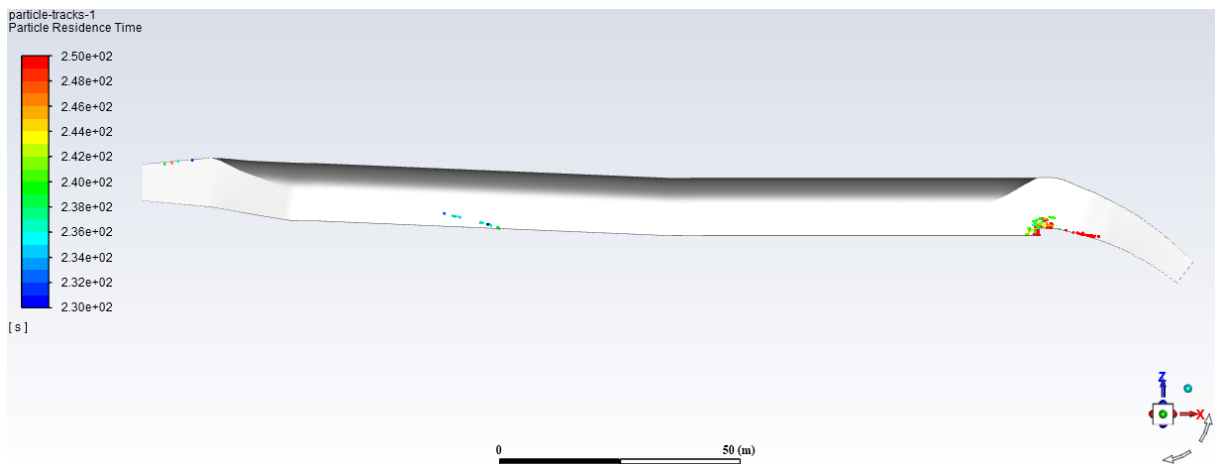


Figure 45: Injection of 0.3 mm particles - after 250 s.

The following figure shows the particles in the open and closed sand trap at the end of the simulations, that is, after 300 s.

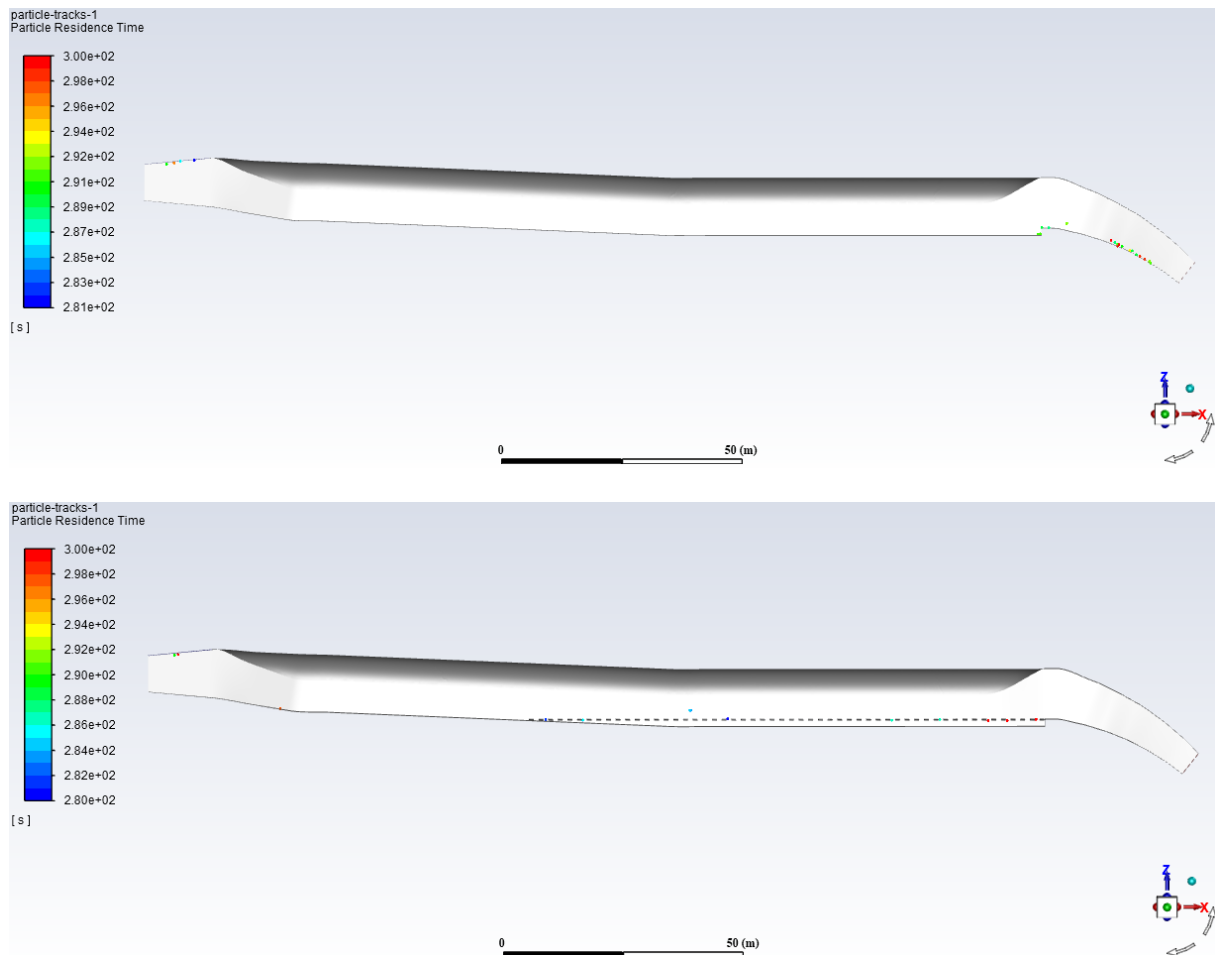


Figure 46: Injection of 0.3 mm particles - after 300 s (end of simulation).

The effect of installing horizontal shear plates in Sand trap 3 at Tonstad power plant can clearly be seen in the time step 215 s after initializing the simulations. Fig 47 presents the placement of the particles in a longitudinal view after 215 s, while Figure 48 shows the particle trajectories for the same time step in plan view.

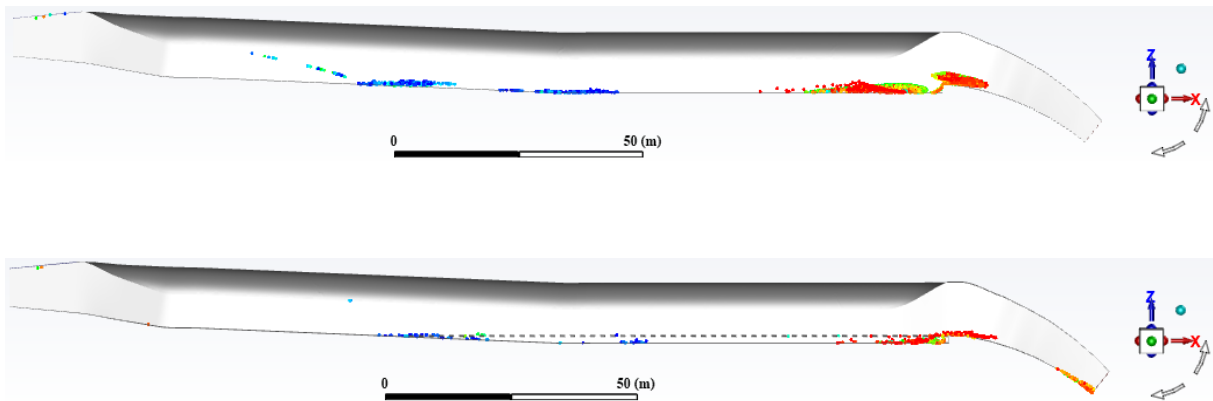


Figure 47: Sediments left in the tunnel after 215 s (longitudinal view).

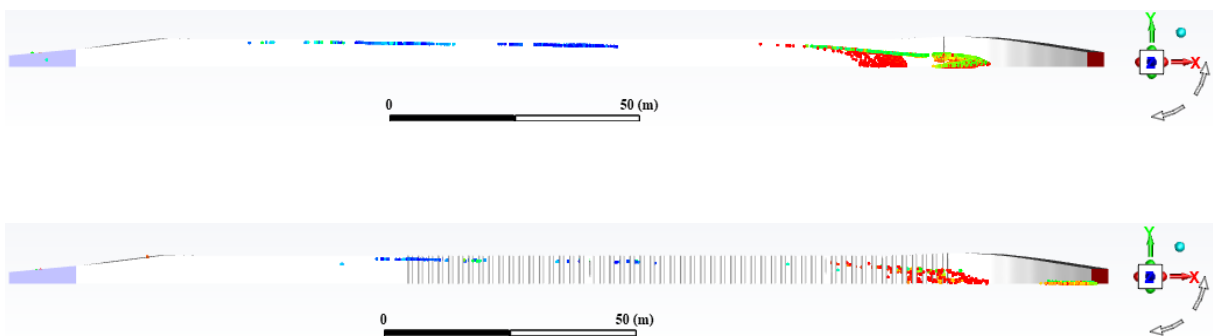


Figure 48: Sediments left in the tunnel after 215 s (plan view).

5.2.3 Sand trap efficiency

By comparing the amount of sediments entering the sand trap over the first 20 s and the amount escaped through the outlet at the end of the simulation, the trap efficiency is calculated by Equation 1. The trap efficiency with and without shear plates for the two particle sizes are given in the following table:

Table 8: Sand trap efficiency.

Particle diameter	1.0 mm	0.3 mm
Trap efficiency (without shear plates)	100 %	87.5 %
Trap efficiency (with shear plates)	100 %	93.4 %

In addition to knowing the trap efficiency, it is interesting to observe the particle trajectories for the open and the closed and trap. The figures presented in subsection 5.2.1 and 5.2.2 shows the particles at different time steps. In addition, a *Solution Animation Play-pack* showing the entire simulation is created for the simulations with 0.3 mm particles. The path of the particles throughout the simulations can then be observed. The MPEG-files attached are named, and the following list explains which file that corresponds to which case:

- “*without-shear-plates-longitudinal*”: Particle trajectories in a longitudinal view without shear plates.
- “*without-shear-plates-plan*”: Particle trajectories in a plan view without shear plates.
- “*with-shear-plates-longitudinal*”: Particle trajectories in a longitudinal view with shear plates.
- “*with-shear-plates-plan*”: Particle trajectories in a plan view with shear plates.

6 Discussion

For the steady state flow simulations, the vector plots show that the velocity decreases close to the bed when horizontal shear plates are installed. Reduced velocity close to the bed in a sand trap is beneficial, both for the settling of particles and for sediments at the bed to stay at rest. By looking at the different plots, it is observed that the velocity in the area immediately upstream the weir is lower for the case with shear plates installed. As shown in section 2.1, sediments are often collected in front of the weir. Reducing the velocity upstream the weir reduces the probability of settled sediments being lifted and transported towards the turbines. The vector plot of the velocity along the bed for the first part of the model shows that the water is flowing backwards. Backflow was also observed in this part in the physical model at the Hydraulic Laboratory at NTNU.

For the transient simulations with sediment injection, the trap efficiency can indicate if reduced velocity with shear plates provides better sand trap performance. For the injection of particles with diameter of 1 mm, the trap efficiency is equal to 100 % both with and without shear plates installed. For this simulation, the only thing that indicates better sand trap performance with shear plates is that all of the sediments are trapped after a shorter time compared to the open sand trap. The trap efficiency is not equal to 100 % when 0.3 mm particles are injected, and the trap efficiency provides information regarding the effect of installing shear plates in Sand trap 3 at Tonstad power plant. The 0.3 mm particle trajectories can be compared to understand the flow pattern of the particles with and without shear plates.

The geometry ranges from downstream the surge tank, where the sediments are injected, to 27 meters downstream the weir. The bend upstream the sand trap is not included and may cause a different inflow, which in turn can have an impact on the sediment flow. Neglecting the access tunnel might also cause the simulation results to differ from the real situation. For the prototype, sediments are transported in the tunnel from the main intake and brook intakes. Thus, sediment injection downstream the surge tank does not represent the real situation. However, the fact that the particles are injected from the top

of the model results in a conservative prediction regarding the trap efficiency. The shear plates are placed in the same height as the weir, but it is possible that it would be more optimal to place the shear plates higher or lower.

The mesh applied for the simulations is the finest mesh that can be generated with the Ansys academic version due to the limitation in number of mesh elements. A finer mesh should be applied to check if the solution is affected. The residuals from the steady state simulation indicates stable converged solutions.

The Reynolds-Averaged Navier-Stokes (RANS) is applied for the modelling of turbulent flow. The approach takes the average effects of turbulence into account instead of the detailed turbulent fluctuations. Several numerical methods could be applied for the modelling of turbulence. Earlier studies have shown that Detached Eddy Simulation (DES) provides better results in turbulent regions. The findings by Sile Almeland et al. (2019) confirms that the solution method has a large impact on the results obtained from CFD computations.

In the simulations, it is assumed that the walls are unlined rock surface for the entire model. In reality, the upstream part of the sand trap and the first part of the pressure shaft downstream the weir is concrete lined. Using a constant roughness height for the walls is therefore a simplification of the model. For the DPM boundary conditions on the walls, the coefficient of restitution is assumed a constant value of 0.9 for both the normal and tangential direction. These values are set based on experience, and it is not tested if the sediment behavior is affected when other values are applied.

7 Conclusion

In this thesis, numerical simulations of Sand trap 3 at Tonstad power plant were carried out using the CFD software Ansys Fluent. The work included creating the model, mesh generation and numerical setup. Further work was done to evaluate the effect of installing horizontal shear plates to improve the trap efficiency at Sand trap 3 at Tonstad hydropower plant.

The steady state Reynolds-Averaged Navier-Stokes simulations without sediment injection were carried out at first. The simulations showed that installing shear plates in the sand trap reduces the velocity along the bed. Reduced the velocity close to the bed should theoretically provide better conditions for particle settling and reduce the entrainment force on the deposited sediments. The transient sediment injection simulations confirmed the findings from the steady flow simulations. For the injection of 1 mm particles, all of the particles are trapped both for the open and the closed sand trap. However, the particles settle faster with shear plates in the sand trap. When 0.3 mm particles are injected, the trap efficiency increases from 87.5 % to 93.4 % when shear plates are installed in Sand trap 3 at Tonstad power plant.

Ansys Fluent is a CFD software capable for the modelling of particles in a pressurized sand trap. The results shows that installing horizontal shear plates increases the trap efficiency for particles with diameters of 0.3 mm. From the results presented, Sira-Kvina power company can be provided with an initial evaluation of the suggested upgrading of the sand trap.

7.1 Proposals for future work

Knowing that Ansys Fluent is a suitable software for simulating particles in a pressurized sand trap, several proposals for future simulations of Sand trap 3 at Tonstad hydropower plant can be presented. The proposals are listed in the following and are further described below.

- Use the commercial version of Ansys Fluent to avoid geometry and mesh limitations.
- Expand the model further upstream and downstream.
- Vary the distance from the bed to the shear plates.
- Perform simulations with a flow calming device at the inlet.
- Apply different numerical methods.
- Use a non-uniform particle diameter distribution and simulate particles smaller than 0.3 mm.

For future work with Sand trap 3 at Tonstad power plant, it is suggested to use the commercial version of Ansys Fluent. The limitation in number of elements is then avoided and it can be evaluated whether a finer mesh affects the solution or not. With the commercial version of the software, the geometry limitations described in section 4.2 are avoided, and the effect of expanding the model further upstream and downstream can also be included in the simulations. If the geometry is expanded further upstream, the gate could be included to simulate the effect of installing horizontal shear plates on the emptying and filling of the sand trap. The upstream bend can also be included. Further, the distance from the bed to the shear plates should be varied to find the optimum height of the shear plates. Another suggestion is to include the access tunnel and perform simulations with a flow calming device at the inlet.

Different numerical methods and smaller time step size can be applied in the simulations to investigate if the solution changes. Other values for the coefficient of restitution should also be tested to check the effect on the particle settling. Another proposal is to use a non-uniform diameter distribution for the injection of sediments. A representation showing the amount trapped for different particle diameters can then be displayed, for example in a histogram. Simulations of particles smaller than 0.3 mm should be performed. The particle size where the shear plates do not improve the sand trap efficiency could then be found.

8 References

AIAA (1998) *Guide for the Verification and Validation of Computational Fluid Dynamics Simulations*, AIAA G-077-1998.

Almeland, S. K. et al. (2019) *Multiple solutions of the Navier-Stokes equations computing water flow in sand traps*. Engineering Applications of Computational Fluid Mechanics, 13(1): 199-219.

Anderson, J. D. (1995) *Computational Fluid Dynamics: The Basics with Applications*. New York: McGraw-Hill Book Company.

Ansys Fluent, *Ansys Fluent Theory Guide*. Ansys Fluent 2019R3.

Bråtveit, K. and Olsen, N. R. B. (2015) *Calibration of Horizontal Acoustic Doppler Current Profilers by three dimensional CFD simulations*. Engineering Applications of Computational Fluid Dynamics, 9(1): 41-49.

Brevik, O. (2013) *3D numerisk modellering av deler av vannvegen til Tonstad kraftverk*. MSc. thesis. Trondheim: NTNU, Department of Hydraulic and Environmental Engineering.

Camp, T. R. (1936) *A study of the Rational Design of Settling Tanks*. Sewage Works Journal, 8(5): 742-758.

Dey, S (2014) *Fluvial Hydrodynamics: Hydrodynamic and Sediment Transport Phenomena*. Berlin: Springer.

Eggen, A. (1973) *Sandtransport og sandfang i kraftverkstunneler*. Trondheim: NTH, Vassdrags- og havnelaboratoriet.

Ingersoll, A. C., McKee, J. E. and Brooks, N. H. (1956) *Fundamental concepts of rectangular settling tanks*. Transactions of the American Society of Civil Engineers, 121(1): 1179-1204.

Jones, W. P and Launder, B. E (1972) *The prediction of laminarization with a two-equation model of turbulence*. International Journal of Heat and Mass Transfer, 15(2): 310-314.

Lysne, D. K. (1969) *Movement of sand in tunnels*. Journal of the Hydraulics Division, 95(6): 1835-1846.

Lysne, D. K. (1971) *Sand transport and sand traps in hydro power tunnels*. International Conference on Pumped Storage Development and Its Environmental Effects.

Lysne, D. K. (1986) *Sand in tunnels*. Senior course in hydropower engineering. Beijing: Tsinghua University.

Lysne, D. K. et al. (2003) *Hydropower development. Vol. no. 8: Hydraulic Design*. Trondheim: NTNU, Department of Hydraulic and Environmental Engineering.

NVE (2010) *Vassdragshåndboka*. Trondheim: Tapir akademisk forlag.

Olsen, N. R. B. (2017) *Numerical Modelling and Hydraulics*. 5th edition. Trondheim: NTNU, Department of Hydraulic and Environmental Engineering.

Paschmann, C (2018) *Design optimization of desanding facilities for hydropower schemes*. Dr.Sc. dissertation. Zurich: ETH Zurich.

Patankar, S. V. (1980) *Numerical Heat Transfer and Fluid Flow*. New York: McGraw-Hill Book Company.

Ranga Raju, K. G. et al. (1999) *Sediment Removal Efficiency of Settling Basins*. Journal of Irrigation and Drainage Engineering, 125(5): 308–314.

Richter, W., Vereide, K. and Zenz, G. (2017) *Upgrading of a Norwegian pressurized sand trap combined with an open air surge tank*. Geomechanics and Tunnelling, 10(5): 620-624.

Roalkvam, B. (2013) *Sandfang i tunneler – Tømming under drift*. MSc. thesis. Trondheim: NTNU, Department of Hydraulic and Environmental Engineering.

Schwimmer, R. (2012) Available at:

<https://serc.carleton.edu/NAGTWorkshops/sedimentary/activities/14100.html>

(accessed: 11.02.2020).

Vassdragsregulantenenes forening (1984) *Sandslitasje på vannkraftturbiner: Kilder og tiltak*. Trondheim: Vassdragsregulantenenes forening.

Vereide, K. et al. (2017) *Upgrading of Sand Traps in Existing Hydropower Plants*. Trondheim: NTNU.

Vereide, K., Svingen, B. and Guddal, R. (2015) *Case study: Damaging effects of increasing the installed capacity in an existing hydropower plant*. Proceedings, 12th International Conference on Pressure Surges, Fluid Transients and Water Hammer. Ireland: Dublin.

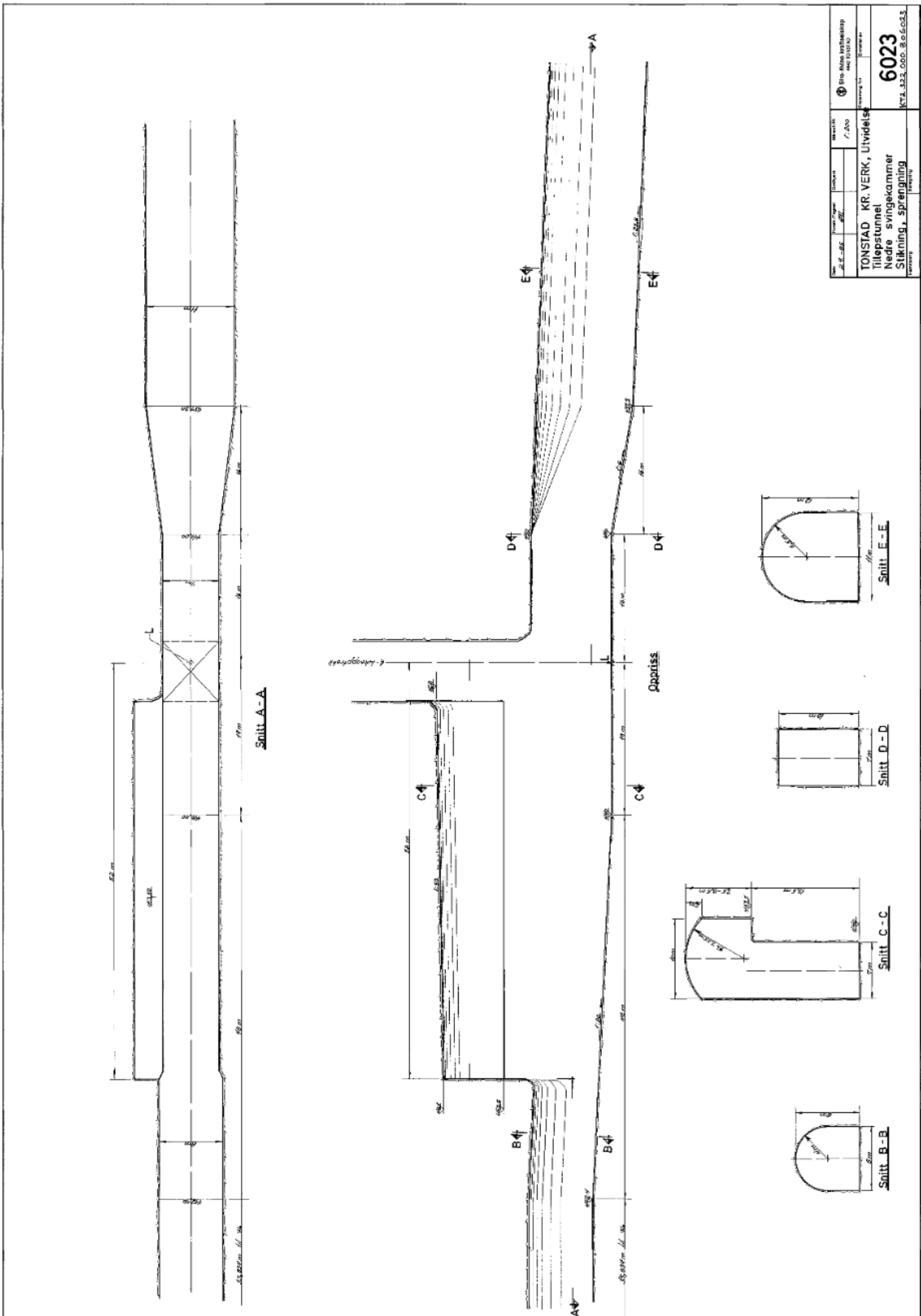
Versteeg, H. K. and Malalasekera, W. (2007) *An Introduction to Computational Fluid Dynamics: The Finite Volume Method*. 2nd edition. Harlow: Pearson Education Limited.

Appendix

Appendix A

Construction drawings

The construction drawings used for creating the geometry are shown on the following pages.



Prosjekt	Byggetype	Bygghet	Bygghet
6023	6023	6023	6023
TONSTAD KR. VERK, Utvidelse Tillepstunnel Nedre svingekammer Sikklings, Sprengning			
6023 KT 1.123, CBS, B.6.603.3			6023

